


# Pressure-driven evolution in the electronic bonding properties of MgO in the super-Earth interior up to $\sim 4$ TPa via core-electron excitation spectroscopy: *Ab initio* calculations

Yoo Soo Yi <sup>1</sup> and Sung Keun Lee <sup>1,2,\*</sup>

<sup>1</sup>Laboratory of Physics and Chemistry of Earth and Planetary Materials, School of Earth and Environmental Sciences, Seoul National University, Korea

<sup>2</sup>Institute of Applied Physics, Seoul National University, Korea

 (Received 19 October 2023; revised 8 May 2024; accepted 21 June 2024; published 9 July 2024)

The discovery of the super-Earth bodies has increased the need to understand planet-forming materials at extremely high pressures, crucial for insights into planetary formation and interior dynamics. Recent progress in high-pressure core-electron excitation spectroscopy, such as x-ray Raman scattering (XRS) experiments, and theoretical calculations offer an opportunity to investigate the evolution of the electronic structures of various compressed materials under such extreme pressure conditions. Despite its significance in planetary and condensed matter physics, the electronic structure of MgO, a major component of super-Earths and a prototypical ionic compound, have not yet been fully studied at pressures corresponding to the deep interiors of super-Earth bodies due to the experimental challenges. Here, we present a theoretical investigation of the XRS spectra, band structures, electron localization functions (ELFs), and Bader charges of MgO at pressures up to  $\sim 4$  TPa. The XRS patterns show the pressure-driven changes in XRS spectral shape and the emergence of new peaks with different slopes (with respect to density and interatomic distances), resulting from enhanced interatomic interactions (i.e., enhanced hybridization between O  $2p$  and Mg  $3s$ - $3p$  states and between adjacent O  $2p$  states). The calculated results are characterized with a pressure-driven delocalization of the unoccupied O  $p$  and Mg  $p$  states, revealing the electronic bonding behavior of MgO under extreme compression, far beyond the current experimental limit with XRS of  $\sim 200$  GPa. The ELF analysis provides a comprehensive understanding of the factors driving the nonlinear trend of absorption edge onset in the calculated XRS patterns and the direct-to-indirect band gap transition of MgO under compression. Together with the Bader charge analysis, it also shows how MgO undergoes a pressure-induced bonding transition from ionic to mixed ionic-covalent without a structural phase transition. This transition of the bonding behavior of MgO under extreme ionic compression contributes to our understanding of material properties under extreme conditions relevant to the interiors of super-Earths. The current result for the prototypical ionic compound under extreme densification offers insights into deepening the fundamental understanding of ionic compounds under extremely high pressures. As the extreme pressure conditions of the current simulations cannot yet be reached in experiment, our breakthrough would be useful to guide future experimental efforts aimed at uncovering metal oxides with pressure-tunable electronic properties.

DOI: [10.1103/PhysRevB.110.035127](https://doi.org/10.1103/PhysRevB.110.035127)

## I. INTRODUCTION

The discovery of super-Earths with a much larger radius ( $R$ ) and mass ( $M$ ) necessitates information of planetary materials under extreme pressure much higher than those for Earth (the pressure at the center of the Earth is  $\sim 360$  GPa). For example, Kepler-22b (with  $\sim 2.1 R_{\oplus}$  and  $\sim 9.1 M_{\oplus}$ ,  $\oplus$  denoting Earth) is expected to have temperatures and pressures ranging from  $\sim 4000$  to  $6000$  K and  $\sim 2000$  to  $2500$  GPa ( $\sim 2$ – $2.5$  TPa) near the core-mantle boundary (CMB) [1] (see Ref. [2] for details about Kepler-22b). Our understanding of the nature of planet-forming materials under such extreme conditions is still in its early stages. Recent theoretical studies have shed light on the behavior of MgSiO<sub>3</sub>, a major component of rocky planets [3], under such extreme conditions. At pressures

above  $\sim 1.1$  or  $2.3$  TPa, comparable with the CMB pressures of Kepler-22b [1], MgSiO<sub>3</sub> is predicted to dissociate into CsCl-type magnesium oxide (MgO) and cotunnite-type SiO<sub>2</sub> [4,5]. Thus, the knowledge of the thermodynamic stability and electronic structures of MgO under extremely high pressures is needed to infer the physical processes in the interiors of these massive rocky planets. The pressure dependence of electronic structures of MgO is expected to affect the thermal and electrical conductivities of mantle materials, providing a perspective on the thermal evolution of massive terrestrial planets ([3,6] and references therein). In addition to its relevance to planetary science, unraveling the electronic structures of metal oxides, key components of optoelectronic devices, at both ambient and extreme conditions has been the target of condensed matter physics and materials physics. Specifically, MgO has a wide range of technologically important applications, as an insulating layer in magnetic tunnel junctions used in hard-disk drive and magnetoresistive random-access memory [7–11].

\*Contact author: sunglee@snu.ac.kr

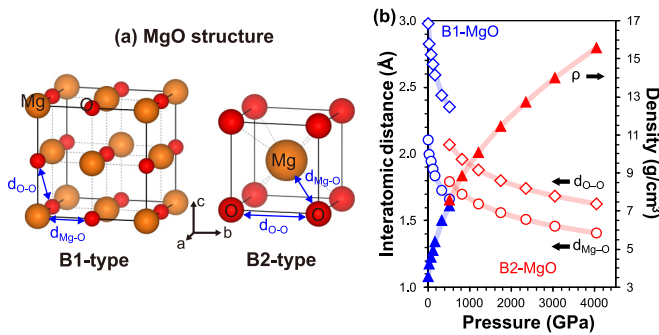


FIG. 1. (a) NaCl-like B1-type and CsCl-like B2-type MgO structures. (b) Variations in the interatomic distance between the nearest-neighboring Mg and O atoms ( $d_{\text{Mg-O}}$ , open diamonds), that between the next-nearest-neighboring O atoms ( $d_{\text{O-O}}$ , open circles), and the density ( $\rho$ , triangles) of B1- and B2-MgO (blue and red, respectively) with varying pressure.

Its stability over a wide range of pressures up to terapascal pressure conditions makes MgO as a model ionic compound, rendering an opportunity to delve into the bonding nature of compressed metal-oxygen ionic bonds under both low and extremely high pressures.

The nature of MgO under pressure has been explored both experimentally and theoretically. Low-pressure MgO, known as the B1 phase with a NaCl-type structure (with 6-coordinated Mg), undergoes a phase transition to a denser CsCl-type structure (with 8-coordinated Mg, the B2 phase) at pressures of  $\sim 500$ – $600$  GPa [12–20]; see Fig. 1 for the MgO structures and Secs. 1 and 2 in the Supplemental Material (SM) [21] (see also Refs. [22–27] therein) for details about the B1-B2 phase transition. The B2-MgO is expected to remain stable at pressures of  $\sim 3$ – $4$  TPa [5,28]. Efforts have been made to elucidate the equation of state [12–18,29–32] and thermal [33–36] and elastic [18,37,38] properties of compressed MgO at elevated temperature and pressure conditions [39,40], with primary implications for the dynamics of Earth’s lower mantle up to  $\sim 150$  GPa (see Sec. 2 in the SM [21] for further details). A previous theoretical study has also identified phase transition pathways of MgO with ZnS-like B3 and B4 structures, NiAs-like B8<sub>1</sub> structure, and hexagonal-BN-like structure [41]. As the stability of those proposed phases (B3, B4, and B8<sub>1</sub>) requires further confirmation [12,42], in this paper, only B1- and B2-type structures at pressures up to the terapascal range are considered.

Despite its significance in both planetary sciences and condensed matter physics and the aforementioned progress in the lattice structures, detailed electronic bonding transitions in MgO under terapascal pressures and their impact on its physical properties have been poorly understood. This is largely due to the experimental challenges in achieving extreme conditions within rocky planets and difficulties in directly probing electronic structures under such extreme conditions. One way to directly probe the electronic structure of oxides under compression is x-ray Raman scattering (XRS, aka nonresonant inelastic x-ray scattering; e.g., Refs. [43–45] and references therein, see Methods section below for a brief theoretical background). Recent breakthroughs with high-pressure XRS experiments, coupled with a diamond anvil cell (DAC), can

reveal the element-specific local electronic structures, particularly bonding environment and the unoccupied partial density of states (PDOS), of various planet-forming materials under high pressures up to 200 GPa (see Refs. [43,46–49] and references therein). For instance, previous experimental studies investigated the XRS signals of low- $Z$  matters under extreme high pressures, such as the B  $K$ -edge and O  $K$ -edge for B<sub>2</sub>O<sub>3</sub> glasses up to 119.4 and 101.6 GPa, respectively [50,51], the O  $K$ -edge for MgSiO<sub>3</sub> glasses up to 130 GPa [52], the O  $K$ -edge for SiO<sub>2</sub> glasses up to 160 GPa [53], the O  $K$ -edge for GeO<sub>2</sub> glasses up to 148 GPa [48], and the C  $K$ -edge for diamond up to 200 GPa [49]. *Ab initio* calculations of XRS spectra were also carried out for the high-pressure crystalline counterparts and melt configurations to interpret the XRS patterns obtained from these experiments (see Ref. [47] and references therein): Briefly, from B<sub>2</sub>O<sub>3</sub>-I at 1 atm to B<sub>2</sub>O<sub>3</sub>-II at 120 GPa [50]; enstatite, and bridgmanite, and postbridgmanite (MgSiO<sub>3</sub>) from 20 to 120 GPa [52,54]; and high pressure  $\alpha$ -PbO<sub>2</sub>-type at 120 GPa [47,53]; from quartz-type GeO<sub>2</sub> at 1 atm to pyrite-type GeO<sub>2</sub> at 300 GPa [48]; and diamond up to 200 GPa [49]. These studies have shown that the formation of highly coordinated network forming cations and oxygens and the increased interatomic proximity (e.g., decreases in O–O) in those phases at high pressure [47–55] affect the overall XRS spectral patterns.

Despite efforts and advancements, *in situ* high-pressure XRS experiments are currently limited to pressures  $< 200$  GPa for various low- $z$  oxides, with no experimental data available beyond this threshold [49], while theoretical insights have extended our understanding up to 300 GPa [48]. With advances in high-pressure DAC capability under extreme pressure conditions up to  $\sim 500$  GPa and higher (see Ref. [56] and references therein), the XRS experiment could be feasible under such extreme compression. Therefore, further theoretical study of XRS spectral patterns of planetary materials beyond the current pressure limit (of 200 GPa) is anticipated. Considering these developments, in this paper, we aim to investigate the detailed electronic structures and the corresponding XRS spectrum of MgO under pressures using *ab initio* calculations.

In contrast with the comprehensive understanding obtained from XRS studies for various oxides and diamond in which covalent bonding is predominant, the systematic studies for compressed ionic compounds are still insufficient; there are a few XRS studies on ionic compounds at 1 atm and low-pressure conditions, such as nitrogen  $K$ -edge XRS of crystalline lithium nitride (Li<sub>3</sub>N) and aluminum nitride (AlN) up to 40 and 33 GPa, respectively [57–59]. As far as we are aware, MgO under high pressures has not been systematically investigated through high-pressure XRS experiments. Previous experimental and theoretical core-electron excitation spectroscopy, including x-ray absorption near-edge structure (XANES), for MgO was carried out at ambient pressure [60–64]. The extended stability of ionic MgO at high pressure (from 1 atm up to  $\sim 3$ – $4$  TPa; details below) offers a rare opportunity to systematically investigate the effects of pressure-induced changes in interatomic distances (i.e., metal-oxygen) on the bonding properties of ionic compounds.

In addition to the widely adopted O  $K$  edge at elevated pressure conditions (see references above), the Mg  $K$  edge at

high pressure could have the potential to probe the densification of Mg-bearing oxides and diverse earth and planetary materials. Currently, Mg *K*-edge XANES spectra of MgO and Mg-bearing phases have been available only at 1 atm [64–69]. Analyzing the Mg *K*-edge features of MgO at high pressures, in the absence of complicated structural phase transitions within the wide pressure range, is expected to help us understand how the Mg coordination number and the Mg–O distance influence the Mg *K*-edge patterns. In this context, as Mg *K*-edge XRS spectroscopy at high pressure is also currently unavailable, carrying out theoretical Mg *K*-edge core-electron excitation spectroscopy of compressed MgO would provide insights into the behavior of ionic compounds at ambient and low-pressure conditions and under extreme pressures.

In this paper, we explore the impact of pressure on the O and Mg *K*-edge XRS spectra of MgO at high pressures up to 4042 GPa ( $\sim 4$  TPa), far beyond the current pressure limit of high-pressure XRS studies ( $\sim 200$  GPa), using *ab initio* calculations. To delve into detailed electronic configurations involving primary Mg–O bond under compression, we calculated the band structure, PDOS, electron localization function (ELF), and Bader charge, as these are essential to comprehend how the metal (Mg)–oxygen bond evolves under extreme pressure; the band structure and PDOS (detailed in Sec. 3 in the SM [21]; see also Refs. [70–72] therein) provide complementary momentum- and energy-resolved electronic structures to probe the electronic transitions responsible for the characteristic *K*-edge spectral patterns. The ELF and Bader charge allow direct visualization of electron distribution and bonding characters. The information quantifies the nature of electron interactions in metal-oxygen bonds, allowing us to properly interpret the evolution of spectral patterns of core-electron excitation spectroscopy, including XRS. Comprehensive analysis of the XRS patterns and corresponding electronic structures reveals the enhanced interatomic interactions of adjacent Mg–O and O–O pairs with increased electron localization between the interacting atoms. With advances in high-pressure experimental techniques, the current results for MgO under terapascal pressures could serve as a useful guide for investigation of the electronic bonding transitions in the interiors of massive rocky exoplanets.

## II. METHODS

### A. MgO structures at high pressures

The structural information of the high-pressure MgO structures up to 4042 GPa investigated in this paper is summarized in Table S1-1 in the SM [21]; see Sec. 1 in the SM [21] for details. Within the pressure range up to 4042 GPa, MgO is known to exist in NaCl-like B1-type and CsCl-like B2-type structures [5,14,17,20,28]; see Fig. 1(a) for the structures of B1- and B2-type MgO. The crystal structure of B1-MgO at 0 GPa was obtained from x-ray diffraction data reported in a previous study [73]. Then given the experimental evidence of the solid-solid phase transition of MgO from B1 to B2 phase  $\sim 400$ – $600$  GPa using shock compression [12,17] and the theoretical prediction of the B1-B2 phase transition at  $\sim 500$  GPa [13,14,19,74,75], we decreased the lattice param-

eter of B1-MgO from 4.2120 to 3.3239 Å to increase the pressure to 505 GPa (Fig. S1-1 in the SM [21]). The potential presence of other phases between B1 and B2 within this pressure range, such as ZnS-like B3 and B4 structures and NiAs-like B8<sub>1</sub> structure, have not been fully established [12,41,42]. To ensure the reliability and consistency of our calculations, we determined the B1-B2 phase transition threshold by comparing the enthalpies of these structures and found that B1-MgO undergoes a phase transition into B2-MgO at pressures  $> 505$  GPa (see Sec. 2 in the SM [21] for details). As presented in Fig. 1(b), the interatomic distance between the nearest-neighbor Mg and O atoms ( $d_{\text{Mg-O}}$ ) and that of the adjacent O atoms ( $d_{\text{O-O}}$ ) decreased from 2.1060 to 1.6620 Å and from 2.9783 to 2.3504 Å, respectively. The density of B1-MgO also increased from 3.58 to 7.29 g/cm<sup>3</sup>. At 505 GPa, because of the phase transition to the denser B2-MgO (density increasing from 7.29 to 7.58 g/cm<sup>3</sup>),  $d_{\text{O-O}}$  decreased from 2.3504 to 2.0665 Å, while  $d_{\text{Mg-O}}$  increased from 1.6620 to 1.7896 Å [Fig. 1(b)].

A previous study extended the stability region of solid MgO up to  $\sim 2$  TPa using double-shock compression, yet direct structural data of MgO under terapascal pressures remain unavailable [32]. On the other hand, theoretical studies, employing evolutionary crystal structure prediction and *ab initio* thermodynamic integration molecular dynamics, have revealed the stability region of B2-MgO up to  $\sim 3$ – $4$  TPa [5,28]. Based on these theoretical insights, we decreased the lattice parameter of B2-MgO from 2.0665 to 1.6260 Å to increase the pressure from 505 to 4042 GPa (Fig. S1-1 in the SM [21]). Then  $d_{\text{Mg-O}}$  and  $d_{\text{O-O}}$  decreased from 1.7896 to 1.4082 Å and from 2.0665 to 1.6260 Å, respectively. The density of B2-MgO increased from 7.58 to 15.57 g/cm<sup>3</sup> [Fig. 1(b)]. The pressure conditions of MgO were determined from the internal stresses, and these values were adjusted considering the lattice parameter of B1-MgO at a pressure of 0 GPa. We performed geometry optimization calculations with supercell structures larger than  $2 \times 2 \times 2$  for B1-MgO and  $3 \times 3 \times 3$  for B2-MgO within the pressure range investigated in this paper. Further geometry optimization does not result in noticeable structural changes in either B1- or B2-MgO.

### B. Electronic structure calculations

Electronic structures of MgO at high pressures were calculated using CASTEP, which employs a plane-wave basis set with pseudopotentials [76]. The *ab initio* calculations of the electronic structures were conducted with the generalized gradient approximation-based Perdew-Burke-Ernzerhof (GGA-PBE) exchange-correlation functional [77], with a 600 eV cutoff energy for the plane-wave basis set and a  $1.0 \times 10^{-6}$  eV/atom self-consistent field (SCF) tolerance. A Gaussian broadening of 0.4 eV for the full width at half maximum (FWHM) was applied to the PDOS for visibility. For B1-MgO, an  $8 \times 8 \times 8$  Monkhorst-Pack (MP) grid density was used, while denser MP grids of  $16 \times 16 \times 16$  to  $20 \times 20 \times 20$  were used for B2-MgO to reveal the highly delocalized electronic structures. The valence configurations of the O and Mg atoms used for the on-the-fly generated ultrasoft pseudopotentials were  $2s\ 2p$  and  $2s\ 2p\ 3s$ , respectively (with the  $1s$  core state). To prevent core-core

overlap between interacting atoms in the highly compressed MgO structures, core radii of 0.8 and 1.1 a.u. were used for the on-the-fly generation (OTFG) of pseudopotentials. Core-core overlaps did not appear within the pressure range investigated in this paper (Fig. S1-2 in the SM [21]) [5]. The convergences of these parameters were thoroughly assessed. Moreover, we employed the Heyd-Scuseria-Ernzerhof (HSE06) hybrid exchange-correlation functional to further refine the band gaps [78]. The band structure calculations using HSE06 were conducted with a 1600 eV cutoff energy for the plane-wave basis sets, a  $1.0 \times 10^{-6}$  eV/atom SCF tolerance, and  $9 \times 9 \times 9$  MP grid for B1- and B2-MgO. The valence configurations and core radii for the OTFG norm-conserving pseudopotentials used for the calculations with HSE06 were the same as those used for the OTFG ultra-soft pseudopotentials (see Sec. 1 in the SM [21] for details).

### C. XRS theoretical backgrounds and *ab initio* calculations of the spectral patterns

The detailed information regarding XRS processes and scattering cross-section are available in the earlier pioneering studies and the extensive reviews (see Refs. [45,46,79–82] and references therein). Here, only a brief remark on the XRS processes is provided. The XRS spectrum can be determined by double-differential scattering cross-section, which involves the dynamic structure factor  $S(\vec{q}, \omega)$  as follows [46] (details in Eqs. (S1.1)–(S1.3) in the SM [21]); here,  $g$  and  $f$  refer to the ground and final states, respectively:

$$S(\vec{q}, \omega) = \sum_f |\langle f | e^{i\vec{q} \cdot \vec{r}} | g \rangle|^2 \delta(E_g - E_f + \hbar\omega). \quad (1)$$

As the product of the scattering vector ( $\vec{q}$ ) and the position vector ( $\vec{r}$ ) in the transition matrix is substantially  $< 1$  ( $\vec{q} \cdot \vec{r} \ll 1$  at the low- $q$  limit) in the XRS process, the first-order term ( $\vec{q} \cdot \vec{r}$ ) of the transition matrix becomes dominant, and the dynamic structure factor in Eq. (1) can be approximated (dipole approximation) as follows [46]:

$$\begin{aligned} \langle f | e^{i\vec{q} \cdot \vec{r}} | g \rangle &\cong \langle f | g \rangle + i \langle f | \vec{q} \cdot \vec{r} | g \rangle - \frac{1}{2} \langle f | (\vec{q} \cdot \vec{r})^2 | g \rangle + \dots \\ &\approx i \langle f | \vec{q} \cdot \vec{r} | g \rangle, \end{aligned} \quad (2)$$

$$S(\vec{q}, \omega) \approx \sum_f |\langle f | \vec{q} \cdot \vec{r} | g \rangle|^2 \delta(E_g - E_f + \hbar\omega). \quad (3)$$

Under the dipole transition approximation, the transition matrix [Eq. (2)] and hence the dynamic structure factor [Eq. (3)] can also be used to describe the electron scattering within electron energy loss spectroscopy (EELS). Note that the transition matrix for x-ray absorption spectroscopy (XAS) is also like those in XRS and EELS at the low- $q$  limit [46,83] [see Eq. (S1.4) in the SM [21] for further details]. XRS, using hard x rays, is an effective *in situ* experimental probe of a matter compressed within DAC [44,46,49,51–53,84–93] (see Ref. [45] and references therein). Our *ab initio* simulations were conducted using the dipole-approximated transition matrix of EELS [94]. In our previous studies, we highlighted the similarity between the XRS and EELS patterns observed not only in the low- $q$  limit but also within a range including

relatively high- $q$  values from  $1.74 \text{ \AA}^{-1}$  (scattering angle of  $18^\circ$ ) to  $6.11 \text{ \AA}^{-1}$  ( $75^\circ$ ) [43,47,48,50]. Considering our objective to provide insights for future XRS experiments under high pressures, the calculated O and Mg  $K$ -edge core-electron excitation spectra in this paper are referred to as XRS spectra. The calculated XRS spectra also resemble those of the corresponding unoccupied  $p$  states (Fig. S3-1 in the SM [21]). The contribution of the quadrupole and other higher-order transitions might be negligible because MgO is composed of only  $s$  and  $p$  elements.

Here, the O and Mg  $K$ -edge XRS spectra of MgO at high pressure were calculated from the excited-state electronic structure of MgO by applying a  $1s$  core hole to each O and Mg atom which is induced by the inelastic scattering of incident x-ray photons (i.e., a core-hole calculation) [95,96]. The contribution of core electrons was included by applying projector augmented plane-wave reconstruction for the pseudowave function of the excited atom [94,97,98]. After introducing a  $1s$  core hole to the core region of pseudopotentials, we adjust the background charge to ensure the system remains neutral. Sufficiently large supercell structures, containing 96–200 total atoms (see Table S1-1 and Sec. 1 in the SM [21]) were used to minimize interactions between periodically repeated excited O and Mg atoms with  $1s$  core holes (O\* and Mg\* hereafter). The calculated O and Mg  $K$ -edge spectra with supercells  $> 96$  atoms did not present significant differences in both B1-MgO at 0 GPa and B2-MgO at 4042 GPa. The XRS calculations were conducted with a  $3 \times 3 \times 3$  MP grid for calculation efficiency. The results obtained with denser MP grids showed no significant differences (detailed features were screened by the instrumental broadening and core-hole lifetime broadening effects; see also Sec. 1 in the SM [21] and Refs. [99,100] therein). The convergence of XRS features was achieved for supercell size, cutoff energy, MP grid, and core radii of O and Mg used for the on-the-fly generated ultrasoft pseudopotentials. A 0.4 eV of the instrumental broadening parameter (Gaussian broadening for FWHM) was applied to the calculated XRS spectra.

The calculated XRS spectra were shifted using  $1s$  core-electron transition energies ( $E_T$ ), which were determined for each excited-state electronic structure with  $1s$  core holes, thus enabling direct comparisons of the XRS patterns of MgO at different pressures. Here,  $E_T$  refers to the energy required to transit from a  $1s$  core hole to the conduction band minimum, and it was determined from the energy difference between the MgO with and without a  $1s$  core hole, considering the core-level energy difference resulting from the use of pseudopotentials (see Ref. [62] for details). The estimation of  $E_T$  when using all-electron/full-potential methods was also summarized in our previous study [47]. The calculated  $E_T$  values for O and Mg atoms varied from 541.12 to 548.02 eV and from 1317.18 to 1327.81 eV, respectively, within the investigated pressure range. Each calculated XRS spectrum for MgO was shifted by its corresponding  $E_T$  value. Then the O and Mg  $K$ -edge spectra of B1-MgO at 0 GPa were shifted by  $-12$  and  $-8$  eV, respectively, to align best with the experimental results reported in previous studies [62–64]. The other spectra for the high-pressure MgO structures were also shifted by the same amounts. The overall shapes of the calculated XRS spectra for B1-MgO at 0 GPa aligned well with the previous

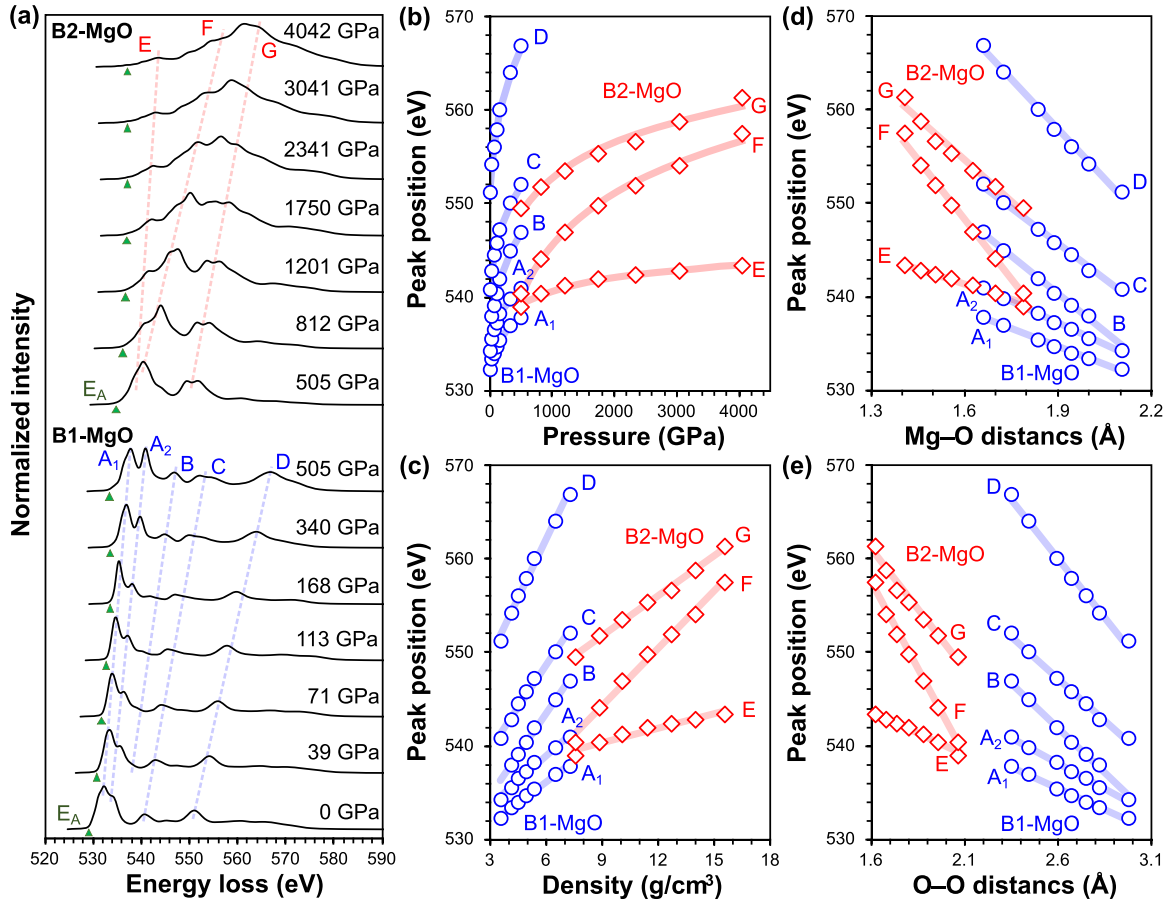


FIG. 2. (a) Calculated O  $K$ -edge x-ray Raman scattering (XRS) spectra for B1- and B2-MgO at high pressures. Shifts of the characteristic peaks are indicated by dashed lines ( $A_1$ – $D$  and  $E$ – $G$  for B1- and B2-MgO, respectively). The absorption edge onsets ( $E_A$ , where the main peak intensity starts to increase) are labeled with triangles. (b)–(e) Variations in the characteristic peak positions with varying pressure, density,  $d_{\text{Mg-O}}$ , and  $d_{\text{O-O}}$ , respectively. The slopes of the characteristic peak shift with varying density near the edge onset ( $\Delta\text{Peak}/\Delta\rho$ ;  $\text{eV g}^{-1} \text{cm}^{-3}$ ), which are determined by assuming a linear relationship between the peak position and density, are as follows: 1.50 for  $A_1$  and 1.80 for  $A_2$  in B1-MgO, and 0.51 for  $E$  and 2.06 for  $F$  in B2-MgO. For the Mg–O distance ( $\Delta\text{Peak}/\Delta d_{\text{Mg-O}}$ ;  $\text{eV}/\text{\AA}$ ),  $-12.70$  for  $A_1$  and  $-15.26$  for  $A_2$  in B1-MgO, and  $-11.01$  for  $E$  and  $-43.28$  for  $F$  in B2-MgO. For the O–O distance ( $\Delta\text{Peak}/\Delta d_{\text{O-O}}$ ;  $\text{eV}/\text{\AA}$ ),  $-8.98$  for  $A_1$  and  $-10.79$  for  $A_2$  in B1-MgO, and  $-9.53$  for  $E$  and  $-37.48$  for  $F$  in B2-MgO.

experimental and theoretical results, which identified main peaks at  $\sim 534$ ,  $\sim 541$ , and  $\sim 551$  eV in the O  $K$ -edge spectrum and at  $\sim 1311$ ,  $\sim 1317$ , and  $\sim 1329$  eV in the Mg  $K$ -edge spectrum [see Figs. 2(a) and 3(a)] [62–64,95,101,102].

### III. RESULTS AND DISCUSSION

#### A. XRS patterns of MgO at high pressures

##### 1. O $K$ -edge XRS spectra

In this section, we investigate changes in XRS patterns of MgO under compression, presented in Figs. 2 and 3. The calculated PDOSs of MgO with and without a  $1s$  core hole at high pressures are also calculated to infer the electronic origins of the XRS pattern (see Sec. 4 and Figs. S3-1–S3-4 in the SM [21]). Figure 2(a) presents the O  $K$ -edge XRS spectra of MgO at high pressures, showing noticeable changes upon compression. The spectrum of B1-MgO at 0 GPa exhibits a main peak at  $\sim 532$  eV (labeled  $A_1$ ), a shoulder peak at  $\sim 533$  eV ( $A_2$ ), and small peaks at  $\sim 542$  eV ( $C$  and  $D$ ).

Previous theoretical studies suggested that the  $A_1$  and  $A_2$  peaks stem from the transition to the antibonding  $O^* 2p$  state hybridized with both Mg  $3s$  and  $3p$  states, and the  $C$  and  $D$  peaks include contributions from the Mg  $3p$  and  $3d$  states, respectively [60,61]. The calculated PDOSs of B1-MgO at 0 GPa in Figs. S3-1 and S3-2 in the SM [21] also confirm hybridizations between the O  $2s$ - $2p$  and Mg  $3s$ - $3p$  states  $\sim 18$  and  $24$  eV. The contribution from the empty Mg  $3d$  state remains unconfirmed because the linear-combination-of-atomic-orbital basis used in our calculations may not fully reveal the contribution from the  $3d$  electron (see Sec. 4 in the SM [21] for further details).

As the pressure increases to 505 GPa, the  $A_1$  and  $A_2$  peaks shift to higher energy and separate into distinct peaks, resulting in a doubletlike feature with peak maxima at  $\sim 537$  and  $\sim 541$  eV. A small shoulder peak appears at  $\sim 538$  eV (labeled  $B$ ) at pressures  $> 39$  GPa and moves gradually to  $\sim 547$  eV with increasing pressure up to 505 GPa. The  $C$  and  $D$  peaks also shift to higher energies and become broader. The doubletlike O  $K$ -edge feature ( $A_1$  and  $A_2$ ), which is like

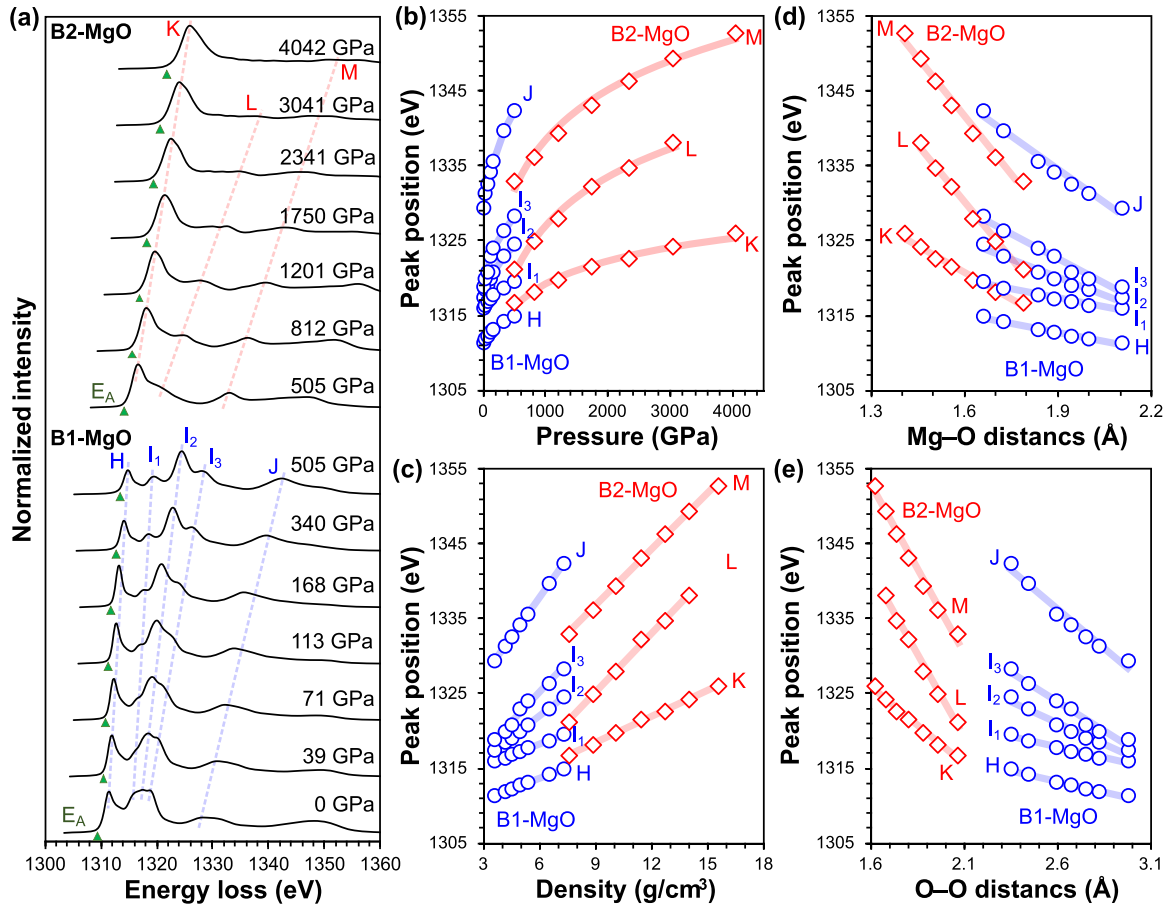


FIG. 3. (a) Calculated Mg  $K$ -edge x-ray Raman scattering (XRS) spectra for B1- and M2-MgO at high pressures. Shifts of the characteristic peaks are indicated by dashed lines (H–J and K–M for B1- and B2-MgO, respectively). The absorption edge onsets ( $E_A$ ) are labeled with triangles. (b)–(e) Variations in the characteristic peak positions with varying pressure, density,  $d_{\text{Mg-O}}$ , and  $d_{\text{O-O}}$ , respectively. The slopes of the characteristic peak shift with varying density near the edge onset ( $\Delta\text{Peak}/\Delta\rho$ ;  $\text{eV g}^{-1} \text{cm}^{-3}$ ), which are determined by assuming a linear relationship between the peak position and density, are as follows: 0.93 for H and 0.95, 1.92, and 2.65 for  $I_1$ ,  $I_2$ , and  $I_3$  in B1-MgO; and 1.15 for K and 2.61 for L in B2-MgO. For the Mg–O distance ( $\Delta\text{Peak}/\Delta d_{\text{Mg-O}}$ ;  $\text{eV}/\text{\AA}$ ),  $-7.81$  for H and  $-7.97$ ,  $-16.03$ , and  $-22.30$  for  $I_1$ ,  $I_2$ , and  $I_3$  in B1-MgO; and  $-24.06$  for K and  $-50.60$  for L in B2-MgO. For the O–O distance ( $\Delta\text{Peak}/\Delta d_{\text{O-O}}$ ;  $\text{eV}/\text{\AA}$ ),  $-5.52$  for H and  $-5.63$ ,  $-11.34$ , and  $-15.77$  for  $I_1$ ,  $I_2$ , and  $I_3$  in B1-MgO; and  $-20.84$  for K and  $-43.82$  for L in B2-MgO.

those of stishovite and other high-pressure  $\text{SiO}_2$  polymorphs (similar features at  $\sim 538$  and  $\sim 544$  eV) [47], would be indicative of the increased oxygen proximity. We confirmed that the changes in  $A_1$ ,  $A_2$ , and B peaks become more evident when the pressure  $> 168$  GPa. Considering the electronic origins of these characteristic peaks discussed above, this suggests that the hybridization between O  $2p$  and Mg  $3s$ – $3p$  states as well as the corresponding antibonding states becomes more pronounced at pressures  $> 168$  GPa. Further details of the electron redistribution between Mg–O bonds will be discussed below (Sec. III C 1).

The phase transition to the denser B2-MgO structure at 505 GPa leads to substantial changes in spectral patterns [Fig. 2(a)], mainly consisting of a shoulder at  $\sim 538$  eV (labeled E) and a characteristic bimodal pattern with peak maxima at  $\sim 540$  and  $\sim 550$  eV (F and G). The PDOSs of B2-MgO with a  $1s$  core hole in Fig. S3-2 in the SM [21] show that the E and F peaks are attributed to the antibonding states of O  $2p$  and Mg  $3s$ – $3p$  hybridizations  $\sim 16$  and  $18$  eV, and the

G peak corresponds to the O  $2p$ –Mg  $3p$  hybridization at  $\sim 28$  eV. The B1–B2 phase transition causes a decrease in  $d_{\text{O-O}}$  from 2.3504 to 2.0665  $\text{\AA}$  but an increase in  $d_{\text{Mg-O}}$  from 1.6620 to 1.7869  $\text{\AA}$  [Fig. 1(b)]. Considering this, these spectral changes are likely a result of enhanced interactions between neighboring oxygen atoms. In the PDOSs of the B2-MgO with a  $1s$  core hole at 505 GPa in Fig. S3-3 in the SM [21], we also observed an increase within the O  $2p$  peak around  $-22$  eV, which is a result of the O  $2p$ – $\text{O}^* 2p$  hybridization. This XRS pattern resembles that of the  $\epsilon$ -phase solid oxygen [90], which has comparable intermolecular oxygen proximity ( $\sim 2.34$   $\text{\AA}$  at 11 GPa and  $\sim 1.96$   $\text{\AA}$  at 94 GPa [103]), also showing bimodal O  $K$ -edge peaks at  $\sim 531$  ( $1s$ – $\pi_g^*$ ) and  $\sim 541$  eV ( $1s$ – $3\sigma_u^*$  transition) due to the intermolecular oxygen  $p$ – $p$  hybridization [90]. As the pressure increases, the F peak shifts to higher energy and merges with the G peak at pressures  $> 1750$  GPa. This feature further shifts to higher energy with increasing pressure to 4042 GPa. At the same time, the E shoulder peak gradually separates from the main peak. The PDOSs of the

B2-MgO with a  $1s$  core hole in Fig. S3-3 in the SM [21] show an increase in the O  $2p$ -O\*  $2p$  hybridization with increasing pressure from 505 to 4042 GPa. This confirms that the observed pressure-induced changes in O  $K$ -edge features of B2-MgO are mainly attributed to an enhanced electronic hybridization between neighboring oxygen atoms. Considering the O and Mg PDOSs of B2-MgO in Fig. S3-2 in the SM [21], these spectral changes also can partly be associated with the increased hybridization between O  $2p$  and Mg  $3s$ - $3p$  states under compression.

## 2. Mg $K$ -edge XRS spectra

Figure 3(a) shows the Mg  $K$ -edge XRS spectra of MgO at high pressures. The Mg  $K$ -edge spectrum of B1-MgO at 0 GPa shows a main peak at  $\sim 1311$  eV (labeled H), a broad feature  $\sim 1316$ - $1318$  eV ( $I_1$ - $I_3$ ), and a small peak at  $\sim 1329$  eV (J). Corresponding PDOSs in Fig. S3-2 in the SM [21] show that these features are primarily attributed to the anti-bonding state of Mg\*  $3p$  hybridized with O  $2s$ - $2p$  and O  $2p$  states (H and  $I_1$ - $I_3$ ), and the unoccupied Mg  $3p$ - $3d$  states (J), respectively [60,61]. As the pressure increases to 505 GPa, several changes are observed. The H peak shifts to higher energy and decreases in intensity. The  $I_1$ - $I_3$  feature splits into three distinct peaks, located  $\sim 1320$ ,  $1324$ , and  $1328$  eV at 505 GPa. The small J peak also shifts to higher energy. Despite the continuous decrease in  $d_{\text{Mg-O}}$  [Fig. 1(b)], these changes in H and  $I_1$ - $I_3$  peaks become more pronounced when the pressure  $> 168$  GPa. This trend at elevated pressures  $> 168$  GPa aligns with the O  $K$ -edge result of B1-MgO presented in Fig. 2(a), implying an enhanced interatomic interaction between Mg and O atoms [ $d_{\text{Mg-O}} > 1.8355\text{\AA}$ ; Fig. 1(b)]. The concurrent spectral changes in both O and Mg  $K$ -edge spectra demonstrate that changes in the unoccupied O  $p$  state coincide with those in the unoccupied Mg  $p$  state through the Mg-O hybridization (Fig. S3-2 in the SM [21]). In addition, these results highlight the influence of Mg-O proximity ( $d_{\text{Mg-O}}$ ) on the Mg  $K$ -edge spectra. Differences in the Mg  $K$ -edge features of Mg-bearing oxides have often been linked to the distinct Mg coordination environment and associated structural distortions [64,66,67]. In the case of B1-MgO, the Mg  $K$ -edge pattern undergoes substantial changes during compression, even in the absence of changes in the coordination environment of Mg.

After the B1-B2 phase transition at 505 GPa, the Mg  $K$ -edge spectrum of B2-MgO shows an intense emerging peak and shoulder at  $\sim 1317$  and  $\sim 1321$  eV (labeled K and L) and a small peak at  $\sim 1333$  eV (M). The PDOSs in Fig. S3-2 in the SM [21] show that these Mg  $K$ -edge features are mainly due to the unoccupied Mg  $3p$  state resulting from the Mg  $3p$ -O  $2p$  hybridization. As the pressure increases from 505 to 4042 GPa, the main peak shifts to higher energy, and its peak width (FWHM) increases from  $\sim 2.8$  to  $\sim 5.1$  eV. At the same time, the L and M peaks gradually disappear with compression. This spectral broadening implies the delocalization of unoccupied Mg  $p$  states as well as the occupied Mg  $3s$ - $3p$  states hybridized with O  $2p$  state, which indicates the enhanced Mg-O interaction under the increased interatomic proximity. The PDOSs of B2-MgO shown in Figs. S3-3 and S3-4 in the SM [21] also support this. Even with the in-

creased proximity, there are no Mg  $K$ -edge XRS features that suggest Mg\*-Mg interactions up to 4042 GPa, as also confirmed from their PDOS patterns (Fig. S3-3 in the SM [21]). These results highlight that the pressure-induced changes in the local electronic structures around O and Mg atoms are well represented in the O and Mg  $K$ -edge XRS features. The pressure-induced evolution of O and Mg  $K$ -edge features reveals a pressure-driven delocalization of the unoccupied O  $p$  and Mg  $p$  states, resulting from enhanced interatomic interactions.

## 3. Phase transition and changes in characteristic XRS patterns

Significant XRS spectral changes are often associated with the phase transition [57-59]. This trend is also apparent in our calculated O and Mg  $K$ -edge XRS spectra for MgO upon phase transition, as presented in Figs. 2(a) and 3(a). Our results also reveal dramatic spectral changes upon compression, even in the absence of the phase transition, within each B1 and B2 phase. To quantify the electronic origins of such a pronounced change in XRS patterns of MgO under extreme compression, we further analyzed how each characteristic peak in the XRS spectra of MgO shifts upon compression. Figures 2(b)-2(e) and 3(b)-3(e) present the variations in the characteristic peak positions for the O and Mg  $K$ -edge results with varying pressure ( $P$ ), density ( $\rho$ ), and interatomic distances ( $d_{\text{Mg-O}}$  and  $d_{\text{O-O}}$ ). In both B1- and B2-MgO, the pressure dependence of each characteristic peak position ( $\Delta\text{Peak}/\Delta P$ ) appears to decrease with increasing pressure [Figs. 2(b) and 3(b)]. Meanwhile, the position of the XRS peak exhibits a linear relationship with both the density ( $\rho$ ) and interatomic distances ( $d_{\text{Mg-O}}$  and  $d_{\text{O-O}}$ ), but it is only valid within the same structural phases [Figs. 2(c)-2(e) and 3(c)-3(e)]. Their slopes show noticeable changes with the phase transition. Values of  $\Delta\text{Peak}/\Delta\rho$ ,  $\Delta\text{Peak}/\Delta d_{\text{Mg-O}}$ , and  $\Delta\text{Peak}/\Delta d_{\text{O-O}}$  near the absorption edge onset are presented in the captions of Figs. 2 and 3. At the B1-B2 phase transition threshold, we also confirmed the emergence of new peaks with different slopes. The results underscore that the significant changes in spectral shape of XRS spectrum and the emergence of new peaks with different slopes (with respect to density and interatomic distances) can be used in future XRS studies to identify the structural phase transitions in MgO and other ionic and covalent oxides.

## B. Band structures of MgO at high pressures

### 1. Absorption edge onset of XRS pattern and band gap

In addition to the XRS peak shifts (Figs. 2 and 3), we also investigated changes in the absorption edge onset ( $E_A$ ) of XRS spectra under compression and compared with the trend of band gap ( $E_G$ ). Here,  $E_A$  refers to the energy at which the main peak begins to increase and is defined as the point where the peak intensity first reaches 5% of the maximum intensity in each spectrum. The  $E_A$  estimates roughly the electronic transition from the core level to the excited-state conduction band minimum [60]. Furthermore, it can be estimated from the experimental spectra (see Refs. [49,54]). Therefore, one can expect that the trends in  $E_A$  under increasing pressure can serve as a practical proxy for understanding the behavior of  $E_G$  of MgO under compression.

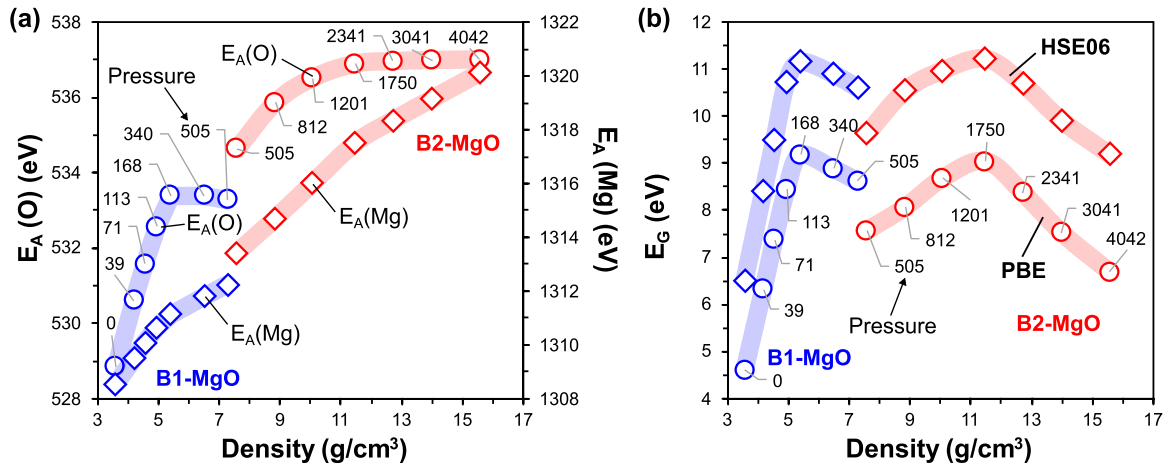


FIG. 4. Variations in (a) the absorption edge energy ( $E_A$ ) of the O and Mg  $K$ -edge x-ray Raman scattering (XRS) spectra in Figs. 2(a) and 3(a),  $E_A(O)$  and  $E_A(Mg)$ , and (b) the band gap ( $E_G$ ) of B1- and B2-MgO with varying density. The band gap calculated with the PBE and HSE06 functionals are presented, with open circles and open diamonds, respectively, for comparison. The pressures corresponding to each density are labeled.

In this paper, the XRS spectra (Figs. 2 and 3) were calculated using the PBE exchange-correlation functional. Although it has successfully captured characteristic XRS patterns and other detailed electronic structures of various oxides at high pressures (see Refs. [47,52] and references therein), it could underestimate band gaps of semiconductors and insulators [104,105]. To address this issue, we also used the HSE06 hybrid exchange-correlation functional, known for its improved representation of nonlocal exchange interactions and more accurate band gap estimation [104,105]. The band gap at 0 GPa calculated using HSE06 is 6.5 eV, closer to the experimentally measured value of  $\sim 7.7$  eV for single-crystal MgO [106]. The band gap with PBE is 4.6 eV, more closely resembling the value of  $\sim 3.8$  eV observed in MgO nanoparticles with reduced band gaps [107,108]. Despite the differences in band gap values, with those calculated using HSE06 being larger than those with PBE by  $\sim 2.2$  eV on average, the pressure dependence of the band gap [Fig. 4(b)] and the characteristic features of band structure remain nearly identical for both functionals (Fig. 5). In the following presentation and discussion, the focus was given to those calculated with HSE06. The results based on the HSE06 functional have been presented in Fig. S1-4 in the SM [21].

Figure 4(a) shows the variations of  $E_A$  for O and Mg, referred to as  $E_A(O)$  and  $E_A(Mg)$ , with varying density, and Fig. 4(b) shows the trend of  $E_G$  of MgO under compression. The  $E_A$  and  $E_G$  exhibit somewhat similar trends, but their detailed behavior is slightly different. For instance,  $E_A(O)$  initially increases from 528.9 to 533.4 eV with increasing pressure up to 168 GPa, then decreases to 533.5 eV under further compression to 505 GPa, and again increases to 534.6 eV associated with the B1-B2 phase transition. On the other hand,  $E_G$  in B1-MgO increases from 6.5 to 11.2 eV up to 168 GPa, then decreases to 10.6 eV with further compression up to 505 GPa, and then experiences a notable drop to 9.6 eV at the B1-B2 phase transition. As the pressure increases, both  $E_A(O)$  and  $E_A(Mg)$  exhibit less pronounced changes; this is accompanied by the broadening of XRS features, which is

attributable to an increased degree of electron delocalization between the interacting atoms (see Ref. [49] for the detailed utility and limitations of  $E_A$  as spectral proxy).

## 2. Direct-to-indirect band gap transition

The band gap of ionic crystals tends to increase upon compression [109]. This is because the localization of valence electrons increases under compression, resulting in a deeper electrostatic potential [109]. However, in our study of MgO under extreme pressures, we confirmed a nonlinear pressure dependence of the band gap, which initially increases and then decreases as the pressure increases. To understand this behavior [109], we present the band structures of high-pressure MgO phases at high pressures from 168 to 1750 GPa in Fig. 5. The calculated band structures reveal that the observed nonlinear behavior of band gap in both B1- and B2-MgO [Fig. 4(b)] can be attributed to a transition from a direct to an indirect band gap. In B1-MgO, the direct-to-indirect band gap transition occurs  $\sim 168$  GPa when the  $X$  valley minimum is lower than the direct  $\Gamma$  valley minimum [Figs. 5(a)–5(c)]. For B2-MgO, the direct-to-indirect band gap transition occurs  $\sim 1750$  GPa when the  $\Gamma$  valley minimum is lower than the direct  $M$  valley minimum [Figs. 5(d)–5(f)]. The observed direct-to-indirect band gap transitions in each B1- and B2-MgO stem from a pressure-induced redistribution of valence electrons between Mg–O and O–O bonds. To elucidate the underlying mechanisms of these transitions, we further examine how compression affects the spatial localization of valence electrons in the section below.

## C. ELFs and Bader charges of MgO at high pressures

### 1. Effect of pressure on the electronic localization in MgO under compression

Figure 6 presents the ELF of MgO at high pressures, directly providing the real-space representation of electron localization. The ELF value ( $N_{\text{ELF}}$ ) at a specific point ( $\vec{r}$ ) is a measure of the ratio between the Pauli kinetic energy density



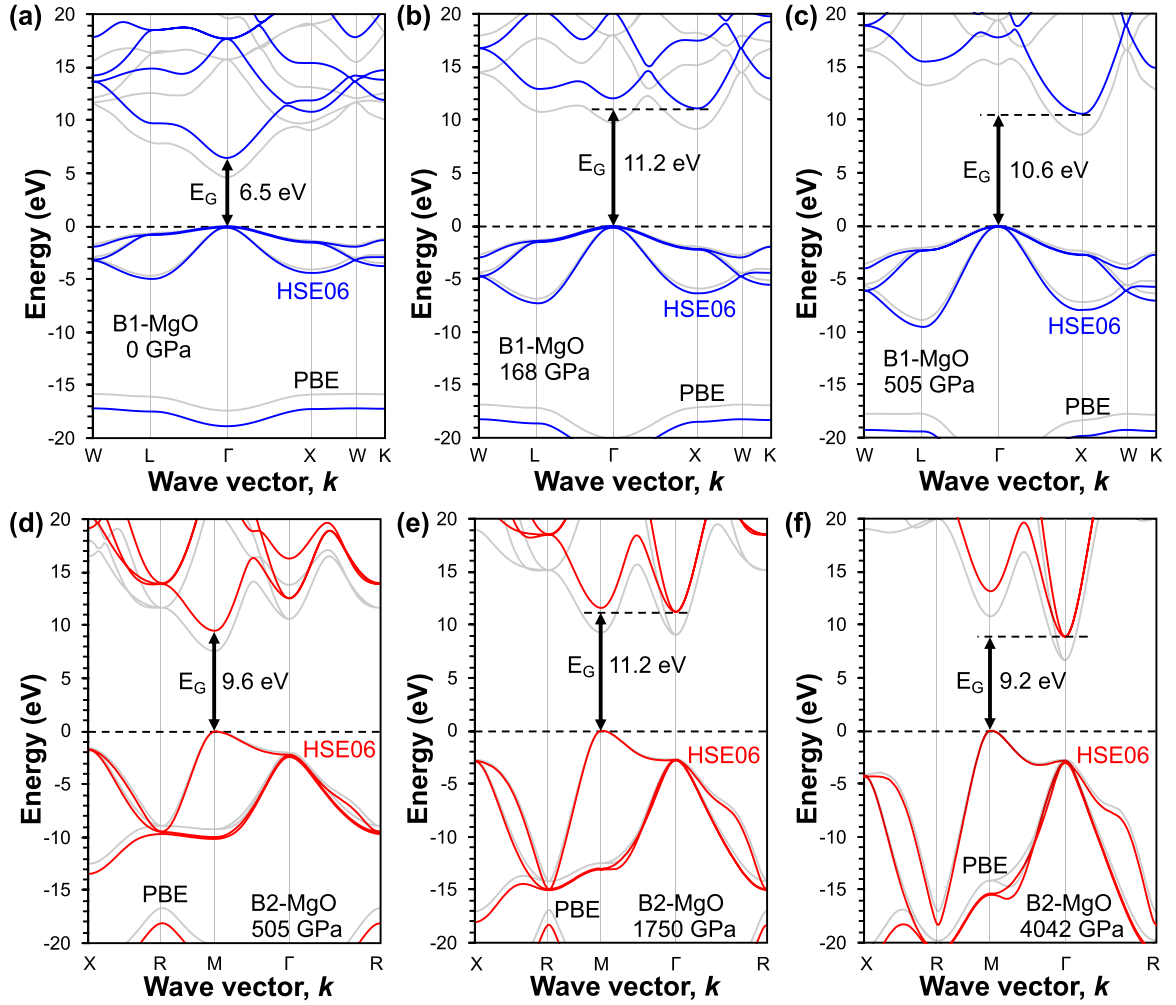


FIG. 5. Calculated band structures for (a)–(c) B1-MgO and (d)–(f) B2-MgO at high pressures (without O\* and Mg\*) along  $W$ - $L$ - $\Gamma$ - $X$ - $W$ - $K$  and  $X$ - $R$ - $M$ - $\Gamma$ - $R$ , respectively. The band structures calculated with HSE06 are depicted with blue and red lines, while those determined with PBE are shown in gray for comparison. The band gap ( $E_G$ ) of each result calculated using HSE06 is labeled. The direct-to-indirect band gap transition thresholds shown in (b) and (e) were determined by a series calculation in which the lattice parameters were decreased by 0.05–0.20 Å in each step.

of the system and that of a homogeneous electron gas [Eq. (4)] [110].

$$N_{\text{ELF}}(\vec{r}) = \frac{1}{1 + [D_\sigma(\vec{r})/D_\sigma^h(\vec{r})]^2}. \quad (4)$$

Here,  $D_\sigma(\vec{r})$  is the Pauli kinetic energy, describing the probability of finding two electrons having the same spin ( $\sigma$ ) based on the Hartree-Fock method, and  $D_\sigma^h(\vec{r})$  is that of a homogeneous electron gas at the same electron density [see Eq. (S2) in the SM [21] and Refs. [111,112] for further details]. The ELF estimates the likelihood of finding an electron in the vicinity of another electron. Thus, unlike the electron density distribution, the ELF provides a representation of the spatial localization of valence electrons between interacting atoms and the nature of chemical bonding in a molecular or solid-state system (see Ref. [111] for how the bonding behaviors of metallic, covalent, and ionic bondings are described using ELF). The ELF ranges from 0 to 1, with values  $\sim 0$  indicating electron delocalization and values  $\sim 1$  indicating electron localization. In our current results, the ELF for the

high-pressure MgO ranges up to 0.83–0.85 since the calculations considered valence electrons only.

The ELF of MgO at 0 GPa in Fig. 6(a) demonstrates the ionic bonding nature of MgO; the highest ELF values are mainly identified near the center of atom, indicating that valence electrons are primarily localized around O and Mg atoms. As the pressure increases to 505 GPa, the shapes of ELF basins for each Mg and O are compressed along the Mg–O and O–O bonding axes with decreasing  $d_{\text{Mg-O}}$  and  $d_{\text{O-O}}$  [Fig. 6(b)]. The phase transition to the denser B2-MgO at 505 GPa leads to a significant reduction in the ELF basins, especially for oxygen atoms, as depicted in Fig. 6(c). Following this trend, a further compression in the directions of Mg–O and O–O bonds is observed as the pressure increases to 4042 GPa [Fig. 6(d)].

To quantitatively elucidate these observed changes in Fig. 6, we further analyzed a pressure-induced evolution in ELF values at a specific point and distances between adjacent ELF basins. Figure 7 presents changes in the ELF values at the saddle points between Mg–O and O–O bonds,

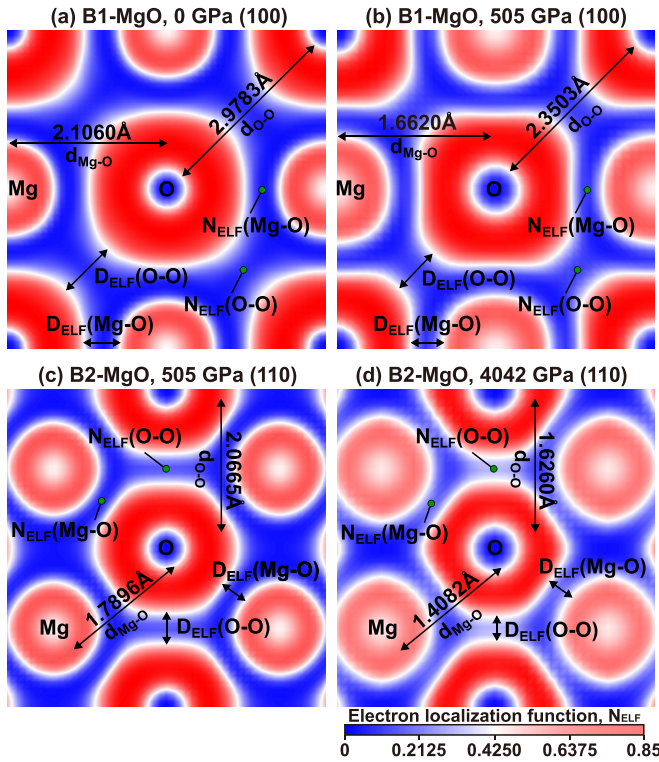


FIG. 6. Calculated electron localization functions (ELFs) for B1- and B2-MgO at high pressures (without  $O^*$  and  $Mg^*$ ), projected onto the (100) and (110) planes as labeled. The atomic sites of Mg and O atoms are labeled with interatomic distances [ $d_{Mg-O}$  and  $d_{O-O}$ ; see Fig. 1(b)]. Positions for determining  $N_{ELF}(Mg-O)$  and  $N_{ELF}(O-O)$  are highlighted with green circles, and the measurement of  $D_{ELF}(Mg-O)$  and  $D_{ELF}(O-O)$  along the Mg-O and O-O bonds are also indicated (details in the text). The projected ELFs are shown from 0 to 0.85. The ELF isosurface of 0.425, represented by the white line, was used to distinguish each ELF basin and to determine  $D_{ELF}(Mg-O)$  and  $D_{ELF}(O-O)$ .

$N_{ELF}(Mg-O)$  and  $N_{ELF}(O-O)$ , with increasing pressure [Figs. 7(a) and 7(b)]. The saddle point between ELF basins represents the boundary between different basins (also called as basin interconnection points) and has been used as a measure of electron localization [112]. The distances between adjacent ELF basins along Mg-O and O-O bonds,  $D_{ELF}(Mg-O)$  and  $D_{ELF}(O-O)$ , were also estimated [Figs. 7(c) and 7(d)]. To determine  $D_{ELF}(Mg-O)$  and  $D_{ELF}(O-O)$ , ELF basins are distinguished by an ELF isosurface of 0.425 (see Fig. 6). For comparison, ELF values in the interstitial region are also presented in Figs. 7(a) and 7(b), but these values remain  $<0.04$  at pressures up to 4042 GPa.

In Fig. 7(a), the electron localizations between Mg-O and O-O bonds of B1-MgO at 0 GPa are negligible as  $N_{ELF}(Mg-O)$  and  $N_{ELF}(O-O)$  are comparable with the ELF value in the interstitial region. The slightly higher  $N_{ELF}(O-O)$  than  $N_{ELF}(Mg-O)$  is because valence electrons from both Mg and O are likely to be localized around the anionic oxygen atoms. As the pressure increases to 505 GPa, the  $N_{ELF}(Mg-O)$  and  $N_{ELF}(O-O)$  of B1-MgO in Fig. 7(a) exhibit nonlinear changes. At lower pressures, both  $N_{ELF}(Mg-O)$  and  $N_{ELF}(O-O)$  increase. However, beyond 168 GPa,  $N_{ELF}(O-O)$  begins

to decrease, while  $N_{ELF}(Mg-O)$  continues to increase. Meanwhile, in Fig. 7(c), the interbasin distances,  $D_{ELF}(Mg-O)$  and  $D_{ELF}(O-O)$ , continuously decrease as the interatomic distances decrease under compression. Note that the direct-to-indirect band gap transition of B1-MgO occurs around this pressure [Fig. 5(b)]. Therefore, this electron redistribution, as evidenced by a significant change in the spatial localization of valence electrons between Mg-O and O-O bonds, plays a crucial role in this band gap transition. This enhanced Mg-O interaction is also consistent with the significant changes observed in the O and Mg  $K$ -edge XRS spectra of B1-MgO at pressures  $>168$  GPa [Figs. 2(a) and 3(a)].

In Fig. 7(b), as  $d_{O-O}$  decreases from 2.3503 to 2.0665 Å upon the B1-B2 phase transition at 505 GPa [Fig. 1(b)],  $N_{ELF}(O-O)$  increases from 0.10 to 0.15, confirming an enhanced O-O interaction. In contrast, a slight decrease in  $N_{ELF}(Mg-O)$  from 0.08 to 0.06 is observed as  $d_{Mg-O}$  increases from 1.6620 to 1.7896 Å [Fig. 1(b)]. This enhanced O-O interaction associated with the B1-B2 phase transition is consistent with the electronic structure inferred from the O  $K$ -edge spectrum of B2-MgO at 505 GPa [Fig. 2(a)], which exhibits the characteristic bimodal pattern due to the intermolecular  $p$ - $p$  hybridization between nearby O atoms [90]. As the pressure further increases to 4042 GPa, both  $N_{ELF}(Mg-O)$  and  $N_{ELF}(O-O)$  in Fig. 7(b) gradually increase from 0.06 to 0.19 and from 0.15 to 0.30, respectively. These results imply the delocalization of valence electrons from Mg and O atoms along the Mg-O and O-O axes. The pressure-induced broadening and peak energy shift in XRS spectra [Figs. 2(a) and 3(a)] are, therefore, reminiscent of the enhanced interactions of both Mg-O and O-O bonds under increased interatomic proximity. The increased  $N_{ELF}(Mg-O)$ , compared with that of B1-MgO at low pressure conditions [Fig. 7(a)], characterized by a pronounced spatial localization of valence electrons between Mg and O atoms, demonstrates the transition of Mg-O bonding from ionic to mixed ionic-covalent character [111].

Figure 7(d) shows that  $D_{ELF}(O-O)$  becomes smaller than  $D_{ELF}(Mg-O)$  at pressures  $>1750$  GPa. This suggests a closer connectivity between adjacent oxygen atoms than between Mg and O atoms, although  $d_{O-O}$  is longer than  $d_{Mg-O}$  in B2-MgO [Fig. 1(b)]. Such a shift in the connectivity of the ELF basins, emphasizing a stronger interaction between adjacent oxygen atoms, appears to underlie the direct-to-indirect band gap transition of B2-MgO observed  $\sim 1750$  GPa [Fig. 5(e)]. Given the dominance of  $N_{ELF}(O-O)$  over  $N_{ELF}(Mg-O)$  and the increased shared-electron interaction [Figs. 7(a) and 7(b)], it is evident that the oxygen-oxygen hybridization becomes increasingly influential in determining the electronic behavior of MgO as the degree of densification increases. To further explore the significance of oxygen-oxygen hybridization, we increased the pressure on B2-MgO up to  $\sim 21$  TPa. While the B2-MgO remains a wide-band-gap insulator up to  $\sim 4$  TPa [Fig. 4(b)], the presence of delocalized valence electrons within the interconnected oxygen layers reduces the band gap, eventually leading to the metallization of B2-MgO at pressures above  $\sim 18$  TPa (see Fig. S3-6 and Sec. 3 in the SM [21] for details; see also Refs. [113–118] therein). This ELF analysis provides a comprehensive understanding of the factors driving the nonlinear trend of absorption edge onset in the calculated XRS patterns and

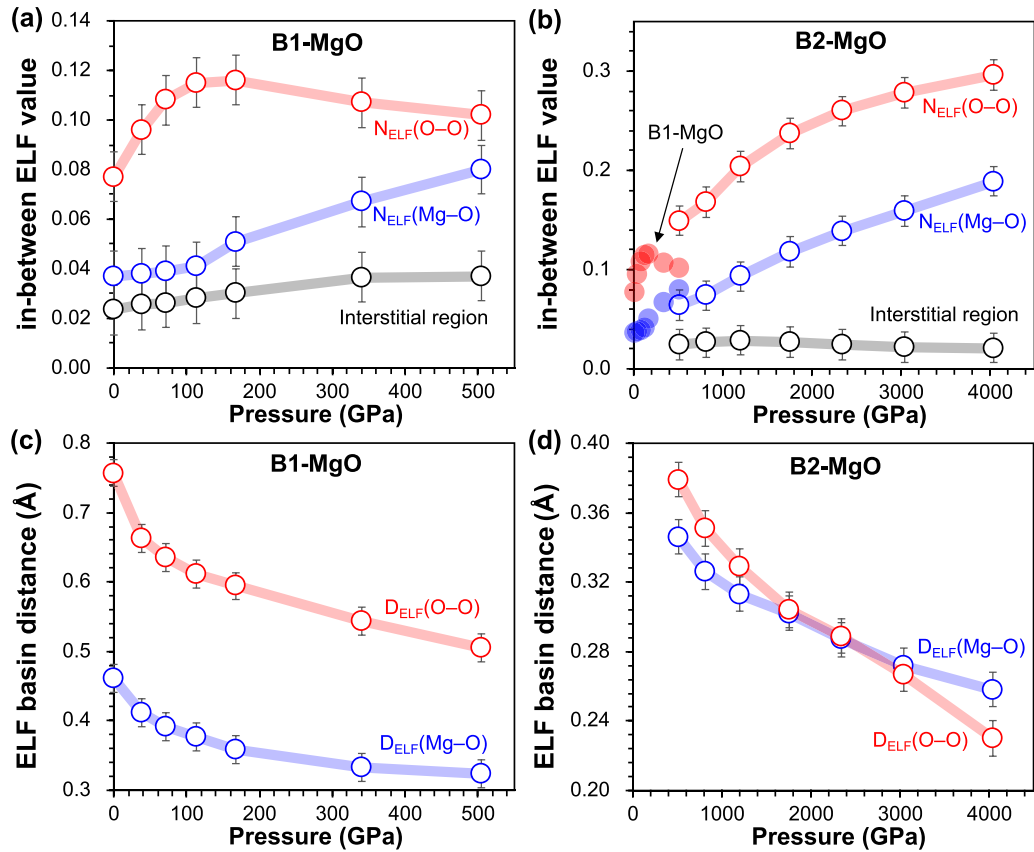


FIG. 7. (a) and (b) electron localization function (ELF) values at the saddle points between Mg–O and O–O bonds,  $N_{\text{ELF}}(\text{Mg-O})$  and  $N_{\text{ELF}}(\text{O-O})$ , determined from the ELF projections in Fig. 6. ELF values at the interstitial region are shown for comparison. Transparent circles in (b) correspond to the result of B1-MgO shown in (a). (c) and (d) Distances between adjacent ELF basins along Mg–O and O–O bonds,  $D_{\text{ELF}}(\text{Mg-O})$  and  $D_{\text{ELF}}(\text{O-O})$ , determined from the ELF projections in Fig. 6. Error bars are included ( $\sim 0.01$  and  $\sim 0.02$  for  $N_{\text{ELF}}$  and  $D_{\text{ELF}}$ ).

the direct-to-indirect band gap transition of MgO under compression (Fig. 4). It also shows how MgO undergoes a pressure-induced bonding transition without a structural phase transition.

We investigated the Bader charges of MgO at high pressures to assess the potential charge transfer between Mg and O atoms [119]. In Fig. 8(a), as the pressure increases up to  $\sim 4$  TPa, the Bader charge for Mg increases from 8.30 to 8.43, while that for O correspondingly decreases from 7.70 to 7.57, exhibiting linear correlations with pressure for each phase. The pressure-induced variations in the Bader charges are more significant in B1-MgO, and it is attributed to the more rapid decrease in the Mg–O distance under compression in B1-MgO compared with B2-MgO [Fig. 1(b)]. At 505 GPa, the Bader charge of Mg slightly decreases from 8.36 to 8.33, and that of O increases from 7.64 to 7.67, associated with an increase in the Mg–O distance from 1.6620 to 1.7896 Å during the B1-B2 phase transition (Fig. 1). The observed charge behavior in Fig. 8(a) suggests an electron transfer from anionic O to cationic Mg under enhanced interatomic proximity, resulting in a more balanced electron distribution between them. Accordingly, as presented in Fig. 8(b), the ionic character of Mg–O bond, which can be characterized by the Bader charge difference, decreases with a reduced

Mg–O distance, exhibiting strong correlations. Together with the XRS and ELF analysis (Figs. 2, 3, and 7), these results of the Bader analysis indicate a transition of the Mg–O bond from a predominantly ionic to a more complex nature, having both ionic and covalent characters. The Mulliken [120] and Hirshfeld [121] results show significant deviations due to their inherent limitations in accurately characterizing systems with ionic character under compression (see Fig. S3-7 and Sec. 3 in the SM [21] for details).

The direct-to-indirect band gap transition in MgO, observed at pressures  $\sim 1.8$  TPa may introduce additional diversity in its properties, especially electrical and thermal conductivity. The electrical conductivity can partly be determined from the band gap and the concentration and mobility of electrons. An increase in a band gap often tends to decrease electrical conductivity [122,123]. The transition at  $\sim 1.8$  TPa, where the band gap decreases after initial increase upon compression, may induce nonlinear increase in the electrical conductivity of MgO. Similarly, thermal conductivity of MgO under compression is expected to be mainly governed by phonon interactions, necessitating future studies regarding phonon-assisted interactions and its impact of the conductivity. Nevertheless, the transition into an indirect band structure and the subsequent decrease in band gap at

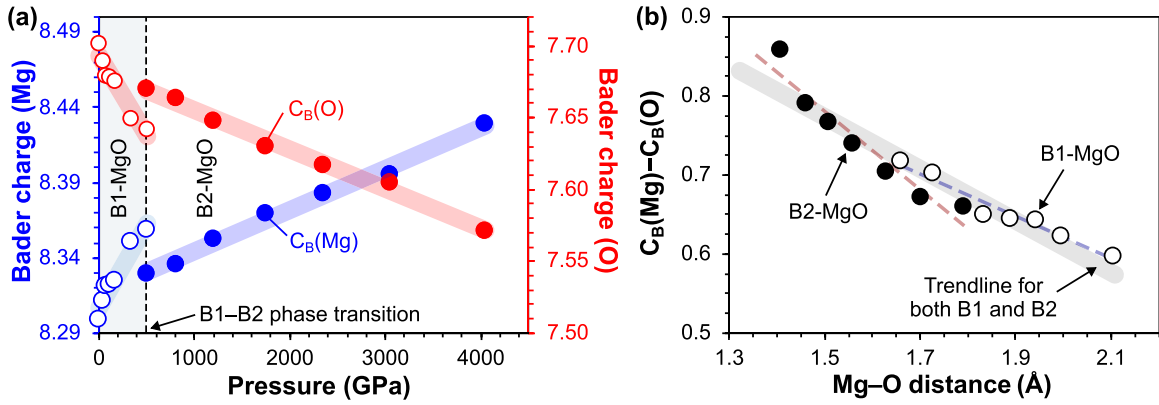


FIG. 8. Variations in (a) the Bader charges ( $C_B$ ) of Mg (blue) and O (red) atoms and (b) the Bader charge difference between Mg and O atoms, i.e.,  $\Delta C_B = C_B(\text{Mg}) - C_B(\text{O})$ , in B1-MgO (open circles) and B2-MgO (closed circles) with varying pressure and Mg-O distance ( $d_{\text{Mg-O}}$ ) as labeled. The valence electron configurations for Mg and O were set to  $2s^2 2p^6 3s^2$  and  $2s^2 2p^4$ , respectively (see Methods). The electron density distributions for the Bader charge analysis were calculated using PBE with higher accuracy (see Fig. S3-7 and Sec. 3 in the SM [21] for details). Linear regression analyses provide trendlines for the Bader charges ( $C_B$ ) vs pressure ( $P$ ):  $C_B(\text{Mg}) = 1.12 \times 10^{-4} P + 8.31$  ( $R^2 = 0.93$ ) and  $C_B(\text{O}) = -1.12 \times 10^{-4} P + 7.69$  ( $R^2 = 0.93$ ) for O of B1-MgO for B1-MgO and  $C_B(\text{Mg}) = 2.74 \times 10^{-5} P + 8.32$  ( $R^2 = 0.99$ ) and  $C_B(\text{O}) = -2.74 \times 10^{-5} P + 7.68$  ( $R^2 = 0.99$ ) for B2-MgO. The trendline of the Bader charge difference ( $\Delta C_B$ ) vs Mg-O distance ( $d_{\text{Mg-O}}$ ) for both B1- and B2-MgO is  $\Delta C_B = -0.33 d_{\text{Mg-O}} + 1.26$  ( $R^2 = 0.90$ ); the trendlines for each phase are  $\Delta C_B = -0.27 d_{\text{Mg-O}} + 1.16$  ( $R^2 = 0.96$ ) for B1-MgO,  $\Delta C_B = -0.50 d_{\text{Mg-O}} + 1.53$  ( $R^2 = 0.93$ ) for B2-MgO.

pressures may result in an increase in the electron contribution to overall conductivity. Such transport properties of compressed MgO under extreme pressure should be investigated in future *ab initio* studies to provide complementary constraints on large-scale thermal processes in the interiors of super-Earth bodies.

#### D. Limitations and practical feasibility

In this paper, we have focused on the pressure-driven evolution in the electronic structure of MgO, yet the effect of temperature on the electronic structures and their impacts on spectroscopic characteristics need to be considered. Under extreme temperature (along with an increase in pressure) conditions in the interiors of super-Earth bodies, the proper inference of the transport properties of highly compressed MgO requires information regarding the thermally induced lattice vibration and its effects to quasiharmonic and anharmonic effects [124]. Compositional complexity within those planetary bodies under such extremely high pressure and temperature conditions should also be further investigated to provide constraints on large-scale thermal processes in the interiors of super-Earth bodies [5,74].

One of the motivations for the current *ab initio* simulations of the electronic structures and calculations of core-electron excitation spectroscopic response from the archetypal metal oxide is that the relevant information is currently unattainable experimentally and may not be feasible in the foreseeable future. The aim of this theoretical paper, therefore, encompasses predicting electronic and spectroscopic properties that are beyond the reach of current experimental capability (e.g.,  $\sim 200$  GPa for O *K*-edge XRS experiments [49]). In line with this challenge, it should be noted again that the XRS experiment tuned for the Mg *K* edge ( $\sim 1300$  eV) is currently challenging even under ambient conditions, as the XRS scat-

tering cross-section decreases dramatically with increasing atomic number. The collection of Mg *K*-edge XRS spectra at high pressure is certainly beyond the current capability, while earlier pioneering efforts with Na *K*-edge XRS (at  $\sim 1071$  eV) shed light on a potential capability (e.g., see Refs. [125,126]). Further improvement in x-ray optics could render us to explore the electronic structures around Mg in oxides under compression *via* Mg *K*-edge XRS. While it remains difficult to predict the experimental feasibility of the edge and the pressure conditions, the progress and advances in XRS over the last two decades have witnessed the opening of opportunities with unreachable pressure conditions and challenging edges. For example, since the inception of XRS for low-*Z* materials at high pressure between 2003 and 2005 [44,51,86,87], for over a decade, acquiring of the XRS signal from compressed condensed matter beyond 100 GPa pressure conditions had been unimaginable [43,91]. Only recently, the XRS spectrum for compressed matter above 100 GPa was reported [50]. Within the last 5 years, the XRS of condensed matter at high pressure up to 200 GPa and beyond, once considered unattainable, has become available [48–50,53,127], highlighting the potential experimental feasibility of challenging XRS experiments to date. Furthermore, irradiation on the Mg  $L_{2,3}$  edge (e.g., Ref. [128]) and relevant *ab initio* calculations for future experiments is crucial, as these features provide insights into local structures beyond the nearest neighbors, complementing the information obtained from *K*-edge features.

Whereas the focus has been given to the pressure-driven evolution of electronic structures of ionic compounds under extreme compression, our Mg *K*-edge XRS results should have immediate practical significance; our Mg *K*-edge results for MgO can be used to account for the effect of metal-oxygen distance on the potential changes in Mg *K*-edge features for other diverse ionic compounds. For example, the systematic shift in Mg PDOS and XRS

patterns with varying Mg–O distance could be a useful proxy to account for the effect of crystalline topology on the PDOS, which requires theoretical investigations. Figure 3(d) shows how a decrease in Mg–O bond length can affect the electronic bonding nature; a decrease in the Mg–O distance ( $d_{\text{Mg-O}}$ ) by 0.1082 Å (from 2.1060 to 1.9978 Å) results in an increase in the main peak positions of the Mg *K*-edge features by 0.55 eV (from 1311.42 to 1311.97 eV) and by  $\sim 1$  eV (from 1317.49 to 1318.47 eV) for the H and I<sub>2</sub> peaks (see also Fig. S3-9 in the SM [21]), respectively. These could make a useful constraint to electronic responses from diverse Mg-bearing ionic compounds at 1 atm and low-pressure conditions, not to mention those under extreme pressure conditions. Since MgO is among the simplest Mg-bearing compounds, the established systematic influence of pressure on the evolution of the electronic structures (both Mg and particularly O *K* edges) of the primary metal-oxygen bond could be applied to study the nature of metal-oxygen bonds (or more broadly, ionic bonds) in any ionic solids.

#### IV. CONCLUSIONS

Given the limited pressure conditions (up to  $\sim 200$  GPa) of the element-specific core-electron excitation spectroscopy experiment of matter under compression, theoretical calculations for predicting and interpreting forthcoming experimental XRS results under much high-pressure conditions have been needed. In this paper, we have investigated XRS spectral patterns, band structures, and ELF of MgO at extremely high pressures up to  $\sim 4$  TPa using *ab initio* calculations. The calculated XRS spectra of MgO under high pressures reveal that the pressure-induced changes in the O and Mg *K*-edge features arise from the enhanced O–O and Mg–O interactions with an increase in the degree of electron localization between these atoms under the increased interatomic proximity. The observed localization of valence electrons between Mg and O atoms suggests a transition of bonding behavior from ionic to mixed ionic-covalent with increased interatomic proximity. The observed changes in the characteristic O *K*-edge features of B2-MgO under compression, along with the increased electron sharing between adjacent O atoms, suggest an increasing

significance of oxygen-oxygen hybridization in determining the electronic behavior of MgO with increasing pressure. Our analysis for the changes in spectral shape and characteristic peak positions of the XRS spectra of MgO under compression demonstrates the potential of this approach to identify structural phase transition and the accompanied changes in electronic structure, such as direct-to-indirect band gap transitions. The direct-to-indirect band gap transition in MgO, observed at pressures  $\sim 1.8$  TPa may introduce additional diversity in its properties, especially electrical and thermal conductivity, while the nature of structural perturbation and responses of MgO under extreme temperature conditions remains.

This high-pressure study of MgO also aligns with the underlying mechanism of the pressure-tunable optoelectronic behavior of ionic compounds [109]. The metal-oxygen bond has often been identified as mainly ionic, yet the nature of the bond under compression is expected to be largely different from those at 1 atm and low-pressure conditions. The influence of pressure on the evolution of the electronic structures of the primary metal-oxygen bond remains unidentified. There has been no comprehensive study into the detailed electronic bonding nature of metal-oxygen bond in ionic compounds under high-pressure environments reaching up terapascal orders. In this paper, we reveal the effect of extreme pressure on the nature of metal-oxygen bonds (or more broadly, ionic bonds) in any ionic solids under compression using *ab initio* simulation. The observed changes in electronic bonding behavior of MgO with the increased interatomic proximity deepen our understanding of the electronic behavior of ionic compounds at high pressures and provide the practical aspects for future theoretical investigations.

#### ACKNOWLEDGMENTS

This paper was supported by the Research Leader program of the National Research Foundation of Korea grants (No. NRF-2020R1A3B2079815) to Sung Keun Lee and the supercomputing resources of the KISTI National Supercomputing Center (No. KSC-2022-CRE-0117). We appreciate three reviewers for their constructive comments, which greatly improved the clarity and quality of this paper.

- 
- [1] C. T. Unterborn and W. R. Panero, The pressure and temperature limits of likely rocky exoplanets, *J. Geophys. Res.: Planets* **124**, 1704 (2019).
  - [2] A. S. Bonomo, X. Dumusque, A. Massa, A. Mortier, R. Bongiolatti, L. Malavolta, A. Sozzetti, L. A. Buchhave, M. Damasso, R. D. Haywood *et al.*, Cold Jupiters and improved masses in 38 Kepler and K2 small planet systems from 3661 HARPS-N radial velocities. No excess of cold Jupiters in small planet systems, *Astron. Astrophys.* **677**, A33 (2023).
  - [3] T. Duffy, N. Madhusudhan, and K. K. M. Lee, in *Treatise on Geophysics (Second Edition)*, edited by G. Schubert (Elsevier, Oxford, 2015), pp. 149–178.
  - [4] K. Umemoto, R. M. Wentzcovitch, and P. B. Allen, Dissociation of MgSiO<sub>3</sub> in the cores of gas giants and terrestrial exoplanets, *Science* **311**, 983 (2006).
  - [5] H. Niu, A. R. Oganov, X.-Q. Chen, and D. Li, Prediction of novel stable compounds in the Mg-Si-O system under exoplanet pressures, *Sci. Rep.* **5**, 18347 (2015).
  - [6] F. W. Wagner, N. Tosi, F. Sohl, H. Rauer, and T. Spohn, Rocky super-Earth interiors, *Astron. Astrophys.* **541**, A103 (2012).
  - [7] W. J. Gallagher and S. S. P. Parkin, Development of the magnetic tunnel junction MRAM at IBM: From first junctions to a 16-Mb MRAM demonstrator chip, *IBM J. Res. Dev.* **50**, 5 (2006).
  - [8] I. Fongkaew, B. Yotburut, W. Sailuam, W. Jindata, T. Thiwatwananikul, A. Khamkongkao, N. Chuewangkam, N. Tanapongpisit, W. Saenrang, R. Utke *et al.*, Effect of hydrogen on magnetic properties in MgO studied by first-principles calculations and experiments, *Sci. Rep.* **12**, 10063 (2022).

- [9] J.-Y. Chen, Y.-C. Lau, J. M. D. Coey, M. Li, and J.-P. Wang, High performance MgO-barrier magnetic tunnel junctions for flexible and wearable spintronic applications, *Sci. Rep.* **7**, 42001 (2017).
- [10] K. Tsunekawa, D. D. Djayaprawira, M. Nagai, H. Maehara, S. Yamagata, N. Watanabe, S. Yuasa, Y. Suzuki, and K. Ando, Giant tunneling magnetoresistance effect in low-resistance CoFeB/MgO(001)/CoFeB magnetic tunnel junctions for read-head applications, *Appl. Phys. Lett.* **87**, 072503 (2005).
- [11] C. N. Rao, U. T. Nakate, R. J. Choudhary, and S. N. Kale, Defect-induced magneto-optic properties of MgO nanoparticles realized as optical-fiber-based low-field magnetic sensor, *Appl. Phys. Lett.* **103**, 151107 (2013).
- [12] F. Coppari, R. F. Smith, J. H. Eggert, J. Wang, J. R. Rygg, A. Lazicki, J. A. Hawreliak, G. W. Collins, and T. S. Duffy, Experimental evidence for a phase transition in magnesium oxide at exoplanet pressures, *Nat. Geosci.* **6**, 926 (2013).
- [13] A. R. Oganov, M. J. Gillan, and G. D. Price, *Ab initio* lattice dynamics and structural stability of MgO, *J. Chem. Phys.* **118**, 10174 (2003).
- [14] A. B. Belonoshko, S. Arapan, R. Martonak, and A. Rosengren, MgO phase diagram from first principles in a wide pressure-temperature range, *Phys. Rev. B* **81**, 054110 (2010).
- [15] R. Musella, S. Mazevet, and F. Guyot, Physical properties of MgO at deep planetary conditions, *Phys. Rev. B* **99**, 064110 (2019).
- [16] F. Soubiran and B. Militzer, Anharmonicity and phase diagram of magnesium oxide in the megabar regime, *Phys. Rev. Lett.* **125**, 175701 (2020).
- [17] R. S. McWilliams, D. K. Spaulding, J. H. Eggert, P. M. Celliers, D. G. Hicks, R. F. Smith, G. W. Collins, and R. Jeanloz, Phase transformations and metallization of magnesium oxide at high pressure and temperature, *Science* **338**, 1330 (2012).
- [18] B. B. Karki, L. Stixrude, S. J. Clark, M. C. Warren, G. J. Ackland, and J. Crain, Structure and elasticity of MgO at high pressure, *Am. Mineral.* **82**, 51 (1997).
- [19] A. R. Oganov and P. I. Dorogokupets, All-electron and pseudopotential study of MgO: Equation of state, anharmonicity, and stability, *Phys. Rev. B* **67**, 224110 (2003).
- [20] Z. Wu, R. M. Wentzcovitch, K. Umemoto, B. Li, K. Hirose, and J.-C. Zheng, Pressure-volume-temperature relations in MgO: An ultrahigh pressure-temperature scale for planetary sciences applications, *J. Geophys. Res.: Solid Earth* **113**, B06204 (2008).
- [21] See Supplemental Material at <http://link.aps.org/supplemental/10.1103/PhysRevB.110.035127> for the additional details on the calculations of core-level excitation features, analysis of density of states, band structures, charge analysis, and others, which includes Refs. [22–27,70–72,99,100,113–118,120,121].
- [22] G. E. Brown, F. Farges, and G. Calas, X-ray scattering and x-ray spectroscopy studies of silicate melts, *Rev. Mineral. Geochem.* **32**, 317 (1995).
- [23] J. Stohr, *NEXAFS Spectroscopy* (Springer, New York, 2003), pp. 8–44.
- [24] M. J. Mehl, R. E. Cohen, and H. Krakauer, Linearized augmented plane wave electronic structure calculations for MgO and CaO, *J. Geophys. Res.: Solid Earth* **93**, 8009 (1988).
- [25] M.-P. Habas, R. Dovesi, and A. Lichanot, The phase transition in alkaline-earth oxides: A comparison of *ab initio* Hartree-Fock and density functional calculations, *J. Phys.: Condens. Matter* **10**, 6897 (1998).
- [26] D. Alfè, Melting curve of MgO from first-principles simulations, *Phys. Rev. Lett.* **94**, 235701 (2005).
- [27] D. Cebulla and R. Redmer, *Ab initio* simulations of MgO under extreme conditions, *Phys. Rev. B* **89**, 134107 (2014).
- [28] T. Taniuchi and T. Tsuchiya, The melting points of MgO up to 4 TPa predicted based on *ab initio* thermodynamic integration molecular dynamics, *J. Phys.: Condens. Matter* **30**, 114003 (2018).
- [29] J.-F. Lin, V. V. Struzhkin, S. D. Jacobsen, M. Y. Hu, P. Chow, J. Kung, H. Liu, H.-k. Mao, and R. J. Hemley, Spin transition of iron in magnesiowüstite in the Earth's lower mantle, *Nature (London)* **436**, 377 (2005).
- [30] J.-F. Lin, A. G. Gavriluk, V. V. Struzhkin, S. D. Jacobsen, W. Sturhahn, M. Y. Hu, P. Chow, and C.-S. Yoo, Pressure-induced electronic spin transition of iron in magnesiowüstite-(Mg,Fe)O, *Phys. Rev. B* **73**, 113107 (2006).
- [31] J.-F. Lin and T. Tsuchiya, Spin transition of iron in the Earth's lower mantle, *Phys. Earth Planet. Inter.* **170**, 248 (2008).
- [32] L. E. Hansen, D. E. Fratanduono, S. Zhang, D. G. Hicks, T. Suer, Z. K. Sprowal, M. F. Huff, X. Gong, B. J. Henderson, D. N. Polsin *et al.*, Melting of magnesium oxide up to two terapascals using double-shock compression, *Phys. Rev. B* **104**, 014106 (2021).
- [33] N. de Koker, Thermal conductivity of MgO periclase at high pressure: Implications for the D' region, *Earth Planet. Sci. Lett.* **292**, 392 (2010).
- [34] S. Stackhouse, L. Stixrude, and B. B. Karki, Thermal conductivity of periclase (MgO) from first principles, *Phys. Rev. Lett.* **104**, 208501 (2010).
- [35] H. Dekura and T. Tsuchiya, *Ab initio* lattice thermal conductivity of MgO from a complete solution of the linearized Boltzmann transport equation, *Phys. Rev. B* **95**, 184303 (2017).
- [36] C. Kwon, Y. Xia, F. Zhou, and B. Han, Dominant effect of anharmonicity on the equation of state and thermal conductivity of MgO under extreme conditions, *Phys. Rev. B* **102**, 184309 (2020).
- [37] C.-S. Zha, H.-K. Mao, and R. J. Hemley, Elasticity of MgO and a primary pressure scale to 55 GPa, *Proc. Natl Acad. Sci. USA* **97**, 13494 (2000).
- [38] S. Ghose, M. Krisch, A. R. Oganov, A. Beraud, A. Bosak, R. Gulve, R. Seelaboyina, H. Yang, and S. K. Saxena, Lattice dynamics of MgO at high pressure: Theory and experiment, *Phys. Rev. Lett.* **96**, 035507 (2006).
- [39] F. Soubiran, F. González-Cataldo, K. P. Driver, S. Zhang, and B. Militzer, Magnesium oxide at extreme temperatures and pressures studied with first-principles simulations, *J. Chem. Phys.* **151**, 214104 (2019).
- [40] F. Soubiran and B. Militzer, Electrical conductivity and magnetic dynamos in magma oceans of super-Earths, *Nat. Commun.* **9**, 3883 (2018).
- [41] K. B. Joshi, B. K. Sharma, U. Paliwal, and B. Barbiellini, Pressure-dependent electronic properties of MgO polymorphs:

- A first-principles study of Compton profiles and autocorrelation functions, *J. Mater. Sci.* **47**, 7549 (2012).
- [42] S. Ting, S. Xiao-Wei, W. Xiao-Ping, O. Yu-Hua, Z. Chun-Lin, G. Peng, and Z. Wei, High-pressure structure prediction and high-temperature structural stability of periclase, *Acta Phys. Sin.* **68**, 126201 (2019).
- [43] S. K. Lee, P. J. Eng, and H.-K. Mao, Probing of pressure-induced bonding transitions in crystalline and amorphous Earth materials: Insights from x-ray Raman scattering at high pressure, *Rev. Mineral. Geochem.* **78**, 139 (2014).
- [44] Y. Q. Cai, H. K. Mao, P. C. Chow, J. S. Tse, Y. Ma, S. Patchkovskii, J. F. Shu, V. Struzhkin, R. J. Hemley, H. Ishii *et al.*, Ordering of hydrogen bonds in high-pressure low-temperature H<sub>2</sub>O, *Phys. Rev. Lett.* **94**, 025502 (2005).
- [45] W. Schulke, *Electron Dynamics by Inelastic X-Ray Scattering* (Oxford University Press, Oxford, 2007), pp. 136–236.
- [46] J.-P. Rueff and A. Shukla, Inelastic x-ray scattering by electronic excitations under high pressure, *Rev. Mod. Phys.* **82**, 847 (2010).
- [47] Y. S. Yi, H. Kim, Y.-H. Kim, and S. K. Lee, Spectral proxies for bonding transitions in SiO<sub>2</sub> and MgSiO<sub>3</sub> polymorphs at high pressure up to 270 GPa by O *K*-edge x-ray Raman scattering, *Phys. Rev. B* **103**, 214109 (2021).
- [48] Y.-H. Kim, Y. S. Yi, H.-I. Kim, P. Chow, Y. Xiao, G. Shen, and S. K. Lee, Pressure-driven changes in the electronic bonding environment of GeO<sub>2</sub> glass above megabar pressures, *J. Am. Chem. Soc.* **144**, 10025 (2022).
- [49] S. K. Lee, Y. Yi, Y.-H. Kim, H.-I. Kim, P. Chow, Y. Xiao, P. Eng, and G. Shen, Imaging of the electronic bonding of diamond at pressures up to 2 million atmospheres, *Sci. Adv.* **9**, eadg4159 (2023).
- [50] S. K. Lee, Y.-H. Kim, P. Chow, Y. Xiao, C. Ji, and G. Shen, Amorphous boron oxide at megabar pressures *via* inelastic x-ray scattering, *Proc. Natl Acad. Sci. USA* **115**, 5855 (2018).
- [51] S. K. Lee, P. J. Eng, H.-k. Mao, Y. Meng, M. Newville, M. Y. Hu, and J. Shu, Probing of bonding changes in B<sub>2</sub>O<sub>3</sub> glasses at high pressure with inelastic x-ray scattering, *Nat. Mater.* **4**, 851 (2005).
- [52] Y.-H. Kim, Y. S. Yi, H.-I. Kim, P. Chow, Y. Xiao, G. Shen, and S. K. Lee, Structural transitions in MgSiO<sub>3</sub> glasses and melts at the core-mantle boundary observed *via* inelastic x-ray scattering, *Geophys. Res. Lett.* **46**, 13756 (2019).
- [53] S. K. Lee, Y.-H. Kim, Y. S. Yi, P. Chow, Y. Xiao, C. Ji, and G. Shen, Oxygen quadclusters in SiO<sub>2</sub> glass above megabar pressures up to 160 GPa revealed by x-ray Raman scattering, *Phys. Rev. Lett.* **123**, 235701 (2019).
- [54] Y. S. Yi and S. K. Lee, Atomistic origins of pressure-induced changes in the O *K*-edge x-ray Raman scattering features of SiO<sub>2</sub> and MgSiO<sub>3</sub> polymorphs: Insights from *ab initio* calculations, *Phys. Rev. B* **94**, 094110 (2016).
- [55] Y. S. Yi and S. K. Lee, Pressure-induced changes in local electronic structures of SiO<sub>2</sub> and MgSiO<sub>3</sub> polymorphs: Insights from *ab initio* calculations of O *K*-edge energy-loss near-edge structure spectroscopy, *Am. Mineral.* **97**, 897 (2012).
- [56] M. I. Erements, V. S. Minkov, P. P. Kong, A. P. Drozdov, S. Chariton, and V. B. Prakapenka, Universal diamond edge Raman scale to 0.5 terapascal and implications for the metallization of hydrogen, *Nat. Commun.* **14**, 907 (2023).
- [57] M. Pravica, N. Bhattacharya, Y. Liu, J. Robinson, W.-S. Au, T. Mizoguchi, Z. Liu, and Y. Xiao, High pressure infrared and x-ray Raman studies of aluminum nitride, *Phys. Status Solidi B* **250**, 726 (2013).
- [58] A. Lazicki, C. W. Yoo, W. J. Evans, M. Y. Hu, P. Chow, and W. E. Pickett, Pressure-induced loss of electronic interlayer state and metallization in the ionic solid Li<sub>3</sub>N: Experiment and theory, *Phys. Rev. B* **78**, 155133 (2008).
- [59] A. Lazicki, B. Maddox, W. J. Evans, C. S. Yoo, A. K. McMahan, W. E. Pickett, R. T. Scalettar, M. Y. Hu, and P. Chow, New cubic phase of Li<sub>3</sub>N: Stability of the N<sup>3-</sup> ion to 200 GPa, *Phys. Rev. Lett.* **95**, 165503 (2005).
- [60] V. Begum, M. E. Gruner, C. Vorwerk, C. Draxl, and R. Pentcheva, Theoretical description of optical and x-ray absorption spectra of MgO including many-body effects, *Phys. Rev. B* **103**, 195128 (2021).
- [61] T. Mizoguchi, K. Tatsumi, and I. Tanaka, Peak assignments of ELNES and XANES using overlap population diagrams, *Ultramicroscopy* **106**, 1120 (2006).
- [62] I. Tanaka and T. Mizoguchi, First-principles calculations of x-ray absorption near edge structure and energy loss near edge structure: Present and future, *J. Phys.: Condens. Matter* **21**, 104201 (2009).
- [63] W. Klysubun, P. Kidkhunthod, P. Tarawarakarn, P. Sombunchoo, C. Kongmark, S. Limpijumngong, S. Rujirawat, R. Yimnirun, G. Tumcharern, and K. Faungnawakij, SUT-NANOTEC-SLRI beamline for x-ray absorption spectroscopy, *J. Synchrotron Radiat.* **24**, 707 (2017).
- [64] S. Yoshioka, K. Tsuruta, T. Yamamoto, K. Yasuda, S. Matsumura, N. Ishikawa, and E. Kobayashi, X-ray absorption near edge structure and first-principles spectral investigations of cationic disorder in MgAl<sub>2</sub>O<sub>4</sub> induced by swift heavy ions, *Phys. Chem. Chem. Phys.* **20**, 4962 (2018).
- [65] J. P. Singh, S. H. Kim, S. O. Won, I.-J. Lee, and K. H. Chae, Atomic-scale investigation of MgO growth on fused quartz using angle-dependent NEXAFS measurements, *RSC Adv.* **8**, 31275 (2018).
- [66] N. Trcera, D. Cabaret, S. Rossano, F. Farges, A.-M. Flank, and P. Lagarde, Experimental and theoretical study of the structural environment of magnesium in minerals and silicate glasses using x-ray absorption near-edge structure, *Phys. Chem. Miner.* **36**, 241 (2009).
- [67] N. Trcera, S. Rossano, K. Madjer, and D. Cabaret, Contribution of molecular dynamics simulations and *ab initio* calculations to the interpretation of Mg *K*-edge experimental XANES in K<sub>2</sub>O–MgO–3SiO<sub>2</sub> glass, *J. Phys.: Condens. Matter* **23**, 255401 (2011).
- [68] T. Yoshimura, Y. Tamenori, N. Iwasaki, H. Hasegawa, A. Suzuki, and H. Kawahata, Magnesium *K*-edge XANES spectroscopy of geological standards, *J. Synchrotron Radiat.* **20**, 734 (2013).
- [69] N. Trcera, D. Cabaret, F. Farges, A. M. Flank, P. Lagarde, and S. Rossano, Mg *K*-edge XANES spectra in crystals and oxide glasses: Experimental vs. theoretical approaches, *AIP Conf. Proc.* **882**, 226 (2007).
- [70] P. E. Blöchl, Projector augmented-wave method, *Phys. Rev. B* **50**, 17953 (1994).
- [71] J. C. Fuggle and S. F. Alvarado, Core-level lifetimes as determined by x-ray photoelectron spectroscopy measurements, *Phys. Rev. A* **22**, 1615 (1980).

- [72] M. O. Krause and J. H. Oliver, Natural widths of atomic  $K$  and  $L$  levels,  $K\alpha$  x-ray lines and several KLL Auger lines, *J. Phys. Chem. Ref. Data* **8**, 329 (1979).
- [73] S. Speziale, C.-S. Zha, T. S. Duffy, R. J. Hemley, and H.-K. Mao, Quasi-hydrostatic compression of magnesium oxide to 52 GPa: Implications for the pressure-volume-temperature equation of state, *J. Geophys. Res.: Solid Earth* **106**, 515 (2001).
- [74] Q. Zhu, A. R. Oganov, and A. O. Lyakhov, Novel stable compounds in the Mg–O system under high pressure, *Phys. Chem. Chem. Phys.* **15**, 7696 (2013).
- [75] J. Bouchet, F. Bottin, V. Recoules, F. Remus, G. Morard, R. M. Bolis, and A. Benuzzi-Mounaix, *Ab initio* calculations of the B1-B2 phase transition in MgO, *Phys. Rev. B* **99**, 094113 (2019).
- [76] S. J. Clark, M. D. Segall, C. J. Pickard, P. J. Hasnip, M. J. Probert, K. Refson, and M. C. Payne, First principles methods using CASTEP, *Z. Kristall.* **220**, 567 (2005).
- [77] J. P. Perdew, K. Burke, and M. Ernzerhof, Generalized gradient approximation made simple, *Phys. Rev. Lett.* **77**, 3865 (1996).
- [78] J. Heyd, G. E. Scuseria, and M. Ernzerhof, Hybrid functionals based on a screened Coulomb potential, *J. Chem. Phys.* **118**, 8207 (2003).
- [79] T. Suzuki, X-ray Raman scattering. Experiment. I, *J. Phys. Soc. Jpn.* **22**, 1139 (1967).
- [80] Y. Mizuno and Y. Ohmura, Theory of x-ray Raman scattering, *J. Phys. Soc. Jpn.* **22**, 445 (1967).
- [81] K. Tohji and Y. Udagawa, X-ray Raman scattering as a substitute for soft x-ray extended x-ray absorption fine-structure, *Phys. Rev. B* **39**, 7590 (1989).
- [82] K. Tohji and Y. Udagawa, Novel-approach for structure-analysis by x-ray Raman-scattering, *Phys. Rev. B* **36**, 9410 (1987).
- [83] F. de Groot, High resolution x-ray emission and x-ray absorption spectroscopy, *Chem. Rev.* **101**, 1779 (2001).
- [84] U. Bergmann, P. Glatzel, and S. P. Cramer, Bulk-sensitive XAS characterization of light elements: From x-ray Raman scattering to x-ray Raman spectroscopy, *Microchem. J.* **71**, 221 (2002).
- [85] S. K. Lee, P. J. Eng, H.-K. Mao, Y. Meng, and J. Shu, Structure of alkali borate glasses at high pressure: B and Li  $K$ -edge inelastic x-ray scattering study, *Phys. Rev. Lett.* **98**, 105502 (2007).
- [86] W. L. Mao, H. K. Mao, P. J. Eng, T. P. Trainor, M. Newville, C. C. Kao, D. L. Heinz, J. F. Shu, Y. Meng, and R. J. Hemley, Bonding changes in compressed superhard graphite, *Science* **302**, 425 (2003).
- [87] Y. Meng, H. K. Mao, P. J. Eng, T. P. Trainor, M. Newville, M. Y. Hu, C. C. Kao, J. F. Shu, D. Hausermann, and R. J. Hemley, The formation of  $sp^3$  bonding in compressed BN, *Nat. Mater.* **3**, 111 (2004).
- [88] J. F. Lin, H. Fukui, D. Prendergast, T. Okuchi, Y. Q. Cai, N. Hiraoka, C. S. Yoo, A. Trave, P. Eng, M. Y. Hu *et al.*, Electronic bonding transition in compressed SiO<sub>2</sub> glass, *Phys. Rev. B* **75**, 012201 (2007).
- [89] H. Fukui, M. Kanzaki, N. Hiraoka, and Y. Q. Cai, X-ray Raman scattering for structural investigation of silica/silicate minerals, *Phys. Chem. Miner.* **36**, 171 (2009).
- [90] Y. Meng, J. Eng Peter, S. Tse John, M. Shaw Dawn, Y. Hu Michael, J. Shu, A. Gramsch Stephen, C.-C. Kao, J. Hemley Russell, and H.-K. Mao, Inelastic x-ray scattering of dense solid oxygen: Evidence for intermolecular bonding, *Proc. Natl Acad. Sci. USA* **105**, 11640 (2008).
- [91] S. K. Lee, J. F. Lin, Y. Q. Cai, N. Hiraoka, P. J. Eng, T. Okuchi, H. K. Mao, Y. Meng, M. Y. Hu, P. Chow *et al.*, X-ray Raman scattering study of MgSiO<sub>3</sub> glass at high pressure: Implication for triclustered MgSiO<sub>3</sub> melt in Earth's mantle, *Proc. Natl Acad. Sci. USA* **105**, 7925 (2008).
- [92] S. K. Lee, P. J. Eng, H. K. Mao, and J. F. Shu, Probing and modeling of pressure-induced coordination transformation in borate glasses: Inelastic x-ray scattering study at high pressure, *Phys. Rev. B* **78**, 214203 (2008).
- [93] P. Wernet, D. Nordlund, U. Bergmann, M. Cavalleri, M. Odellius, H. Ogasawara, L. A. Naslund, T. K. Hirsch, L. Ojamae, P. Glatzel *et al.*, The structure of the first coordination shell in liquid water, *Science* **304**, 995 (2004).
- [94] S.-P. Gao, C. J. Pickard, A. Perlov, and V. Milman, Core-level spectroscopy calculation and the plane wave pseudopotential method, *J. Phys.: Condens. Matter* **21**, 104203 (2009).
- [95] T. Mizoguchi, I. Tanaka, M. Yoshiya, F. Oba, K. Ogasawara, and H. Adachi, Core-hole effects on theoretical electron-energy-loss near-edge structure and near-edge x-ray absorption fine structure of MgO, *Phys. Rev. B* **61**, 2180 (2000).
- [96] C. Hébert, Practical aspects of running the WIEN2K code for electron spectroscopy, *Micron* **38**, 12 (2007).
- [97] S.-P. Gao, C. J. Pickard, M. C. Payne, J. Zhu, and J. Yuan, Theory of core-hole effects in  $1s$  core-level spectroscopy of the first-row elements, *Phys. Rev. B* **77**, 115122 (2008).
- [98] V. Milman, K. Refson, S. J. Clark, C. J. Pickard, J. R. Yates, S. P. Gao, P. J. Hasnip, M. I. J. Probert, A. Perlov, and M. D. Segall, Electron and vibrational spectroscopies using DFT, plane waves and pseudopotentials: CASTEP implementation, *J. Mol. Struct.* **954**, 22 (2010).
- [99] S. Huotari, T. Pylkkanen, J. A. Soininen, J. J. Kas, K. Hamalainen, and G. Monaco, X-ray-Raman-scattering-based EXAFS beyond the dipole limit, *J. Synchrotron Radiat.* **19**, 106 (2012).
- [100] T. T. Fister, G. T. Seidler, C. Hamner, J. O. Cross, J. A. Soininen, and J. J. Rehr, Background proportional enhancement of the extended fine structure in nonresonant inelastic x-ray scattering, *Phys. Rev. B* **74**, 214117 (2006).
- [101] I. Tanaka, T. Mizoguchi, and T. Yamamoto, XANES and ELNES in ceramic science, *J. Am. Ceram. Soc.* **88**, 2013 (2005).
- [102] M. Sinha, M. Gupta, P. Jonnard, and M. H. Modi, Soft x-ray characterization of ion beam sputtered magnesium oxide (MgO) thin film, *Surf. Interface Anal.* **50**, 1145 (2018).
- [103] H. Fujihisa, Y. Akahama, H. Kawamura, Y. Ohishi, O. Shimomura, H. Yamawaki, M. Sakashita, Y. Gotoh, S. Takeya, and K. Honda, O<sub>8</sub> cluster structure of the epsilon phase of solid oxygen, *Phys. Rev. Lett.* **97**, 085503 (2006).
- [104] A. J. Garza and G. E. Scuseria, Predicting band gaps with hybrid density functionals, *J. Phys. Chem. Lett.* **7**, 4165 (2016).
- [105] P. Borlido, J. Schmidt, A. W. Huran, F. Tran, M. A. L. Marques, and S. Botti, Exchange-correlation functionals for band gaps of solids: Benchmark, reparametrization and machine learning, *Npj Comput. Mater.* **6**, 96 (2020).



- [106] M. W. Williams and E. T. Arakawa, Optical properties of single-crystal magnesium oxide, *J. Appl. Phys.* **38**, 5272 (2004).
- [107] M. C. C. Wobbe, A. Kerridge, and M. A. Zwijnenburg, Optical excitation of MgO nanoparticles; a computational perspective, *Phys. Chem. Chem. Phys.* **16**, 22052 (2014).
- [108] N. Kamarulzaman, D. T. Mustafa, N. F. Chayed, N. Badar, M. F. M. Taib, and A. B. M. A. Ibrahim, Comparison of experimental and first-principle results of band-gap narrowing of MgO nanostructures and their dependence on crystal structural parameters, *Appl. Nanosci.* **8**, 1621 (2018).
- [109] J. S. C. Kearney, M. Graužinytė, D. Smith, D. Sneed, C. Childs, J. Hinton, C. Park, J. S. Smith, E. Kim, S. D. S. Fitch *et al.*, Pressure-tunable visible-range band gap in the ionic spinel tin nitride, *Angew. Chem. Int. Ed.* **57**, 11623 (2018).
- [110] A. D. Becke and K. E. Edgecombe, A simple measure of electron localization in atomic and molecular systems, *J. Chem. Phys.* **92**, 5397 (1990).
- [111] K. Koumpouras and J. A. Larsson, Distinguishing between chemical bonding and physical binding using electron localization function (ELF), *J. Phys.: Condens. Matter* **32**, 315502 (2020).
- [112] A. Savin, R. Nesper, S. Wengert, and T. F. Fässler, ELF: The electron localization function, *Angew. Chem. Int. Ed.* **36**, 1808 (1997).
- [113] N. P. Armitage, E. J. Mele, and A. Vishwanath, Weyl and Dirac semimetals in three-dimensional solids, *Rev. Mod. Phys.* **90**, 015001 (2018).
- [114] S. F. Elatresh and S. A. Boney, Stability and metallization of solid oxygen at high pressure, *Phys. Chem. Chem. Phys.* **22**, 12577 (2020).
- [115] J. Sun, M. Martinez-Canales, D. D. Klug, C. J. Pickard, and R. J. Needs, Persistence and eventual demise of oxygen molecules at terapascal pressures, *Phys. Rev. Lett.* **108**, 045503 (2012).
- [116] H. Fukui, T. Anh Le, M. Wada, N. Hiraoka, T. Iitaka, N. Hirao, Y. Akahama, and T. Irifune, Electronic structure of dense solid oxygen from insulator to metal investigated with x-ray Raman scattering, *Proc. Natl Acad. Sci. USA* **116**, 21385 (2019).
- [117] X. Chen and Y. Ma, High-pressure structures and metallization of sodium chloride, *Europhys. Lett.* **100**, 26005 (2012).
- [118] J. L. Feldman, B. M. Klein, M. J. Mehl, and H. Krakauer, Metallization pressure for NaCl in the B2 structure, *Phys. Rev. B* **42**, 2752 (1990).
- [119] G. Henkelman, A. Arnaldsson, and H. Jónsson, A fast and robust algorithm for Bader decomposition of charge density, *Comput. Mater. Sci* **36**, 354 (2006).
- [120] R. S. Mulliken, Electronic population analysis on LCAO-MO molecular wave functions. I, *J. Chem. Phys.* **23**, 1833 (1955).
- [121] F. L. Hirshfeld, Bonded-atom fragments for describing molecular charge densities, *Theor. Chim. Acta* **44**, 129 (1977).
- [122] J. Liu, J. Yan, Q. Shi, H. Dong, J. Zhang, Z. Wang, W. Huang, B. Chen, and H. Zhang, Pressure dependence of electrical conductivity of black titania hydrogenated at different temperatures, *J. Phys. Chem. C* **123**, 4094 (2019).
- [123] M. Rütten, M. Kaes, A. Albert, M. Wuttig, and M. Salinga, Relation between bandgap and resistance drift in amorphous phase change materials, *Sci. Rep.* **5**, 17362 (2015).
- [124] X. Tang and J. Dong, Pressure dependence of harmonic and anharmonic lattice dynamics in MgO: A first-principles calculation and implications for lattice thermal conductivity, *Phys. Earth Planet. Inter.* **174**, 33 (2009).
- [125] L. M. de Kort, M. Lazemi, A. Longo, V. Gulino, H. P. Rodenburg, D. Blanchard, C. Sahle, M. Sundermann, H. Gretarsson, A. M. J. van der Eerden *et al.*, Deciphering the origin of interface-induced high Li and Na ion conductivity in nanocomposite solid electrolytes using x-ray Raman spectroscopy, *Adv. Energy Mater.* **14**, 2303381 (2024).
- [126] K. P. Nagle, G. T. Seidler, E. L. Shirley, T. T. Fister, J. A. Bradley, and F. C. Brown, Final-state symmetry of Na 1s core-shell excitons in NaCl and NaF, *Phys. Rev. B* **80**, 045105 (2009).
- [127] Y.-H. Kim, P. Chow, Y. Xiao, G. Shen, and S. K. Lee, Electronic bonding transitions in oxide glass above two megabar pressures, *Phys. Rev. Res.* **6**, L022051 (2024).
- [128] C. J. Sahle, S. Kujawski, A. Remhof, Y. Yan, N. P. Stadie, A. Al-Zein, M. Tolan, S. Huotari, M. Krisch, and C. Sternemann, *In situ* characterization of the decomposition behavior of Mg(BH<sub>4</sub>)<sub>2</sub> by x-ray Raman scattering spectroscopy, *Phys. Chem. Chem. Phys.* **18**, 5397 (2016).